Title
Iroquois Homeobox Gene 3 Establishes Fast Conduction in the Cardiac His-Purkinje Network

Author
Zhang, Shan-Shan

Publication Date
2010

Peer reviewed|Thesis/dissertation

Iroquois Homeobox Gene 3 Establishes Fast Conduction in the Cardiac His-Purkinje Network

by

Shan-Shan Zhang

DISSERTATION

Submitted in partial satisfaction of the requirements for the degree of

DOCTOR OF PHILOSOPHY

in

Biomedical Sciences

in the

GRADUATE DIVISION

of the

UNIVERSITY OF CALIFORNIA, SAN FRANCISCO

Dedication

To my wonderful husband Matt, family, and friends.

Acknowledgements:

Graduate school could not have been such a fulfilling experience without the support from my mentor and supervisor Dr. Benoit Bruneau. Dr. Bruneau is a brilliant scientist who has taught me patience and perseverance, and instilled in me the knowledge, confidence, and drive needed as I continue on my path in research.

I am very grateful for my committee members Drs. Brian Black, Takashi Mikawa, and Jeffrey Olgin. Their constructive criticism and guidance have helped shape my academic as well as personal growth over the years. I would also like to take this opportunity to thank Lisa Magargal and Monique Piazza. They have made graduate school such an enriching experience along each step of the way. I will never forget sitting down and meeting with Brian and Lisa in their offices for the first time (within days of first arriving in San Francisco). Their kindness and warmth melted away my worries, and encouraged me to venture forward.

During graduate school, I have had the pleasure to cross paths with so many wonderful people. My labmates are an amazing bunch – I have counted on them for advice, critique, support, and sometimes just some plain old fun. I am truly happy and grateful to be in an environment where such a diverse group of people can work together to face challenges and reach common goals. I would especially like to thank John Wylie and Dr. Jamie Smyth for their encouragement and words of wisdom that have made these years an unforgettable experience.

Lastly, I would like to acknowledge that all of this could not have been possible without the support from my loving husband Matthew Wheeler and my family. Mom,

dad, Adam, David, Wendy, aunty Gina, and Hartmut – thank you for giving me the strength to keep moving forward in life and reach for my dreams.

Data presented was initially submitted for publication in *Nature* entitled, *Iroquois homeobox gene 3* establishes fast conduction in the cardiac His-Purkinje network by Zhang SS*, Kim K-H*, Rosen A*, Smyth JW*, Sakuma R*, Delgado-Olguín P, Davis M, Chi NC, Puviindran V, Gaborit N, Sukonnik T, Wylie JN, Brand K-A, Farman G, Kim J, Rose RA, Marsden PA, Zhu Y, Zhou Y-Q, Miquerol L, Henkelman MR, Stainier DYR, Shaw RM, Hui C-C, Bruneau BG, Backx PH.

Contributions:

Under the guidance and supervision of Dr. Bruneau, Zhang SS contributed significantly to this large body of work. The connexin studies were undertaken in close collaboration with Smyth JW. Data presented in Figures 12-14, 20, 23, 25, and 26 were generated by the remaining authors, who have given permission for their inclusion in this thesis.

***Iroquois Homeobox Gene 3* Establishes**
Fast Conduction in the Cardiac His-Purkinje Network

Shan-Shan Zhang

With each heartbeat, impulses generated by the sinoatrial node travel through the atria, pause at the atrioventricular node, and proceed to the ventricular conduction system (VCS), also known as the His-Purkinje network. Rapid electrical conduction in the VCS tightly controls spatiotemporal mechanical activation of the ventricles, thereby optimizing pump function. Conduction through the VCS is impaired in several inherited forms of cardiac conduction disorders and associated with increased risk of arrhythmias and heart disease. Although regulation of early specification and patterning of this tissue is becoming better understood, less is known about how transcriptional regulation establishes fast conducting properties of its constituent cells. Using a combination of approaches including mouse genetics, 3D imaging, electrophysiology, cell and molecular biology, we show that the *Iroquois homeobox gene 3* is critical for efficient impulse conduction and ventricular activation in mice and zebrafish. Specifically, loss of *Irx3* in mice resulted in disruption of the rapid and coordinated spread of ventricular excitation, decreased cellular excitability, and altered intercellular coupling. We detected decreased levels of Cx40 in the conduction axis and ectopic Cx43 expression in the proximal bundle branches. We show that Irx3 directly represses *Gja1* (encoding Cx43) transcription and indirectly activates *Gja5* (encoding Cx40). Our results reveal a novel role for Irx3 in the regulation of impulse propagation and ventricular conduction system function.

TABLE OF CONTENTS

LIST OF FIGURES

INTRODUCTION

I. The Mammalian Ventricular Conduction System

In response to integrated networks of molecular cues, a simple linear heart tube matures to form a multi-chambered functional unit that sustains life. Integral to this process is the development of the cardiac conduction system (CCS), which establishes and coordinates the heartbeat. The specialized myocytes of the ventricular conduction system (VCS), also known as the His-Purkinje network, are essential for fast impulse conduction in the ventricles. The histologically distinct His-Purkinje system was first described and studied by the Czech physiologist Jan Evangelista Purkyně in 1839, and by the Swiss cardiologist Wilhelm His, Jr. in 1893 (Silverman et al. 2006).

With each heartbeat, electrical impulses generated by the sinoatrial node (SAN) travel through the atria, pause at the atrioventricular node (AVN), and proceed to the VCS (Figure 1). The VCS is further subdivided into the common bundle of His (atrioventricular bundle), bifurcating bundle branches along the interventricular septum (IVS) that make connections with the ventricular free walls, and a subendocardial network of Purkinje fibers (Miquerol et al. 2004; Aanhaanen et al. 2010). Rapid impulse conduction in this fast conduction axis tightly controls the spatiotemporal activation of the ventricles to optimize heart muscle pumping function (Cohen et al. 1968).

II. Determinants of Impulse Conduction Efficiency

Each cardiac impulse, which is conducted as waves of excitation measurable as action potentials (APs), is propagated from one myocyte (source) to the next (sink)

through intercellular gap junctions (Kleber and Rudy 2004). The efficiency of impulse propagation through the His-Purkinje network is determined by the source-sink relationships between cells, which in turn is dependent on the interplay between cell and tissue morphology, membrane excitability, and electrical coupling of adjacent cells via gap junctions (Rudy and Shaw 1997) (Figure 2).

Tissue morphology

The VCS is a highly intricate and asymmetric network of cells, which are distinct from nodal and working myocytes in shape and size. They are found as oval and cylindrical cells bundled into fascicles along their longitudinal axis (Viragh and Challice 1982; Mikawa and Hurtado 2007). The overall VCS structure is highly conserved in mammals, including humans and mice (Miquerol et al. 2004). In the mouse, Miquerol and colleagues showed that the common His bundle, which is continuous with the AV node and surrounded by fibrous insulation, further branches into about twenty or more smaller bundles along the left septal flank. However, only one or two branches run along the right septal side. These bundles continue to ramify toward the base to form two dense web-like networks of large and interlaced fascicles along the IVS and the free ventricular walls.

Excitability

Cells of different regions of the heart vary in their ability to generate and propagate action potentials and must be integrated and controlled by specialized

myocytes of the CCS. The peacemaking cells of the SAN generate the initial impulse by depolarizing surrounding atrial myocytes. The traveling impulse is then delayed at the AVN, to allow time for atrial relaxation, before rapidly firing down the electrically insulated VCS. This fast conducing pathway is essential for effectively directing the ventricular muscle to contract in a controlled apex-to-base sequence.

Cells of the VCS have the ability to spontaneously generate an action potential (known as automaticity), a faster rate of depolarization, and longer action potential durations compared to ventricular working myocytes (Schram et al. 2002; Miquerol et al. 2004). These excitability characteristics are determined by the expression pattern, level, and kinetics of various voltage-gated ion channels and the currents they encode (Shaw and Rudy 1997; Rudy 1998; Rudy 2005). The adult VCS in humans and mice is enriched in genes encoding several pore-forming and auxiliary subunits of sodium channels such as *Scn5a* and *Scn1b* (Gaborit et al. 2007; Remme et al. 2009). How the expression patterns and levels of these genes are transcriptionally regulated in the maturing VCS is an area of active investigation.

Intercellular Coupling

Gap junctions represent a low resistance pathway for current flowing from one cell to the next, thus directing the spread of the electrical impulse throughout the heart. Each gap junction channel is made up of a pair of abutting connexons from adjacent cell membranes (Miquerol et al. 2003). Each connexon is comprised of 6 connexins (Cxs) which, depending on the isoform present, dictate channel conductance of ion currents and small molecules. Fast conduction velocity in the VCS can be partially explained by the

extensive coupling of constituent cells via the following connexins: Cx40, Cx43, Cx45, and Cx30.2 (Cole et al. 1988; Saez et al. 2003; Kleber and Rudy 2004; Mangoni and Nargeot 2008). The low conductance Cx30.2 and Cx45 are found in the AVN while Cx40 and Cx45 are expressed in the common His bundle and along the bundle branches (van Veen et al. 2001; Kreuzberg et al. 2006). Cx40, Cx43 and Cx45 are all expressed in the distal Purkinje fibers. Changes in their expression pattern, level, and trafficking have been shown to alter channel conductance and conduction efficiency (Jongsma and Wilders 2000). Currently, transcriptional regulation of the precise expression of Cxs in subregions of the VCS tissue remains to be addressed.

III. Relevance to heart disease

Perturbations of normal heart development can lead to congenital heart defects and progressive heart diseases later in life (Hoffman and Kaplan 2002). In particular, impulse propagation through the CCS is impaired in several inherited forms of cardiac conduction disorders and associated with increased risk of arrhythmias and heart disease (Iuliano et al. 2002). In the US, over 250,000 pacemaker implants are performed each year (Mond 2006). Impaired ventricular conduction, which is detectable as prolongation of the QRS interval and bundle branch block by electrocardiography (ECG), can lead to life threatening arrhythmias in diseased hearts (Iuliano et al. 2002; Dhingra et al. 2006). Without a better understanding of the regulatory pathways important for ventricular conduction system function, current treatments, which include anti-arrhythmic drugs and pacemaker implants, are limited and treat those with advanced disease. Although a growing number of VCS-specific genes are being identified, and regulation of early VCS

specification is becoming better understood (Meysen et al. 2007; Moskowitz et al. 2007; Bakker et al. 2008), less is known about transcriptional pathways that dictate how cells of the VCS gain their specialized functional properties.

IV. Iroquois transcription factors

Precise regulation of tissue- and time-specific transcription is key to normal development of the heart (Srivastava 2006). The *Iroquois homeobox* (*Irx*) gene family of transcription factors contain a highly conserved DNA-binding homeodomain of the three amino acid loop extension (TALE) superclass, and are characterized by an 11 amino acid *Iro* motif of unknown function (Figure 3). *Irx* genes have evolutionarily conserved roles during embryonic development, including early tissue patterning as well as later tissue differentiation, and can act as either repressors or activators of gene expression depending on the cellular context (Bruneau et al. 2001; Gomez-Skarmeta and Modolell 2002; Matsumoto et al. 2004; Costantini et al. 2005).

The *Iroquois* family of transcription factors was initially discovered in flies, of which *ara* and *caup* were shown to participate in the patterning of neural and vein precursors, establishment of planar polarity in the eye and wing disc, and dorsal-ventral axis patterning in the ovary (Gomez-Skarmeta et al. 1996; Gomez-Skarmeta and Modolell 1996; McNeill et al. 1997; Kehl et al. 1998; Jordan et al. 2000). Vertebrate studies have also demonstrated their importance in specifying and patterning the neural plate, neural tube, brain, nephron, and lung (Cavodeassi et al. 2001; van Tuyl et al. 2006; Reggiani et al. 2007). Interestingly, all 6 *Irx* genes are expressed in partially overlapping patterns in the developing mouse heart (Christoffels et al. 2000; Cohen et al. 2000;

Bruneau et al. 2001; Mummenhoff et al. 2001; Costantini et al. 2005). While *Irx4* was implicated in chamber specification, *Irx5* was shown to be required for patterning of cardiac repolarization gradient (Bao et al. 1999; Bruneau et al. 2001; Costantini et al. 2005). The functional significance of Irx3 in the heart remains unknown.

V. A role of *Iroquois homeobox gene 3* in the VCS

We examined the developmental expression of Irx3 in mice in which sequences encoding the tauLacZ fusion protein (Callahan and Thomas 1994) were inserted at the translational start site of Irx3 to create a loss-of-function reporter allele (Figure 4). The taulacZ reporter recapitulates endogenous *Irx3* expression in the central nervous system of the developing embryo (Figure 5a). At embryonic day (E) 10, a ring-like group of Irx3tauLacZ^{+} cells was detected in the developing ventricle. These cells represent a subset of developing trabeculae surrounding the emerging IVS and are thought to contribute to the VCS (Christoffels et al. 2000) (Figure 5b). At E14, Irx3^{+} cells were found at the top of the IVS where the bundle of His develops, and as bundles of elongated myocytes along the septum that later become the bundle branches (Viragh and Challice 1982) (Figure 5c).

The adult VCS is highly asymmetric and comprises the bundle of His, bundle branches, and subendocardial Purkinje fibers (Miquerol et al. 2004). Cells expressing Irx3tauLacZ indeed mature into a highly elaborate network, marking the insulated common His bundle (Figure 5e) which branches from the base of the heart toward the apex along the endocardial surface to form a web of interlaced fascicles that make connections with the free wall and septum (Figure 5d,f,g). While a large fan-like group of

small bundles extend along the left septal flank (Figure 5 g), a few thin bundles branch away from the common bundle on the right side (Figure 5 f). The overall architecture of Irx3tauLacZ^{+} cells can be appreciated in images generated by optical projection tomography (OPT). Figures 5 h and i are representative OPT images of Irx3tauLacZ expression in the VCS primordium at E16.5, and the highly intricate His-Purkinje system by postnatal day 3 (P3), respectively.

We obtained a bacterial artificial chromosome (BAC) transgenic line, which encompasses the *Irx3* locus and expressing enhanced green fluorescence protein (EGFP) under 150kb of the 5' regulatory region of *Irx3* from NINDS GENSAT (Figure 5), as a marker line for Irx3-expressing cells. At E14.5, Irx3::EGFP fluorescence recapitulates endogenous Irx3LacZ expression (Figure 5 a-d). Irx3::EGFP-expressing cells were isolated by flow cytometry (FACS) and were shown by qPCR to be enriched in VCS markers, as well as in Irx3 (Figure 5e,f). In contrast, epicardially enriched Kv4.2, was significantly higher in non-GFP samples. These studies showed that the Irx3::EGFP line is a suitable genetic tool for the molecular and cellular analysis of Irx3 and the specialized VCS.

With these initial findings and tools at hand, we set out to try and understand what roles Irx3 could play in the heart. In Chapter 1, we establish that Irx3 is highly enriched in specialized myocytes of the VCS by a combination of gene expression, cell behavior, and lineage tracing studies. We show that Irx3 is co-expressed with VCS markers such as Cx40, Scn5a, and HCN4. In addition, isolated Irx3-expressing cells exhibited higher automaticity than non-expressing cells, and preferentially expressed Cx40 when allowed to reaggregate in culture.

Characterization of the functional significance of Irx3 in the heart is presented in Chapter 2. Along with our collaborators, we undertook a variety of whole heart and animal electrophysiology approaches to show that loss of *Irx3* resulted in abnormally slowed ventricular activation. This conduction defect was characterized by right bundle branch block, which was caused by reduced conduction velocity. We also examined expression of the zebrafish homologs *ziro3a* and *ziro3b* in the heart, and found that *ziro3a,* which is more evolutionarily related to *Irx3*, is highly enriched in the fish ventricle. Knock down studies revealed a conserved requirement for *ziro3a* in ventricular activation.

Using fluorescence imaging, cell behavior, and dye coupling assays, we detected abnormal cellular phenotypes that resulted from loss of Irx3. These results are presented in Chapter 3. Our studies revealed a decrease in cellular excitability and abnormal cell-cell coupling. Specifically, we observed a decrease in Cx40 expression, and ectopic expression of Cx43 in the proximal bundle branches where little expression is normally found. Abnormal communications between the proximal VCS and the working myocardium was tested by dye coupling assays performed in live adult heart slices.

In Chapter 4, we examined how Irx3 functions to regulate the gene expression changes in Cx40 and Cx43. Using adenoviral overexpression of Irx3 in neonatal ventricular myocytes (NVMs), chromatin immunoprecipitation, and luciferase assays, we show that Irx3 is a direct repressor of Cx43 transcription, and an indirect activator of Cx40 expression. Irx3 was shown to directly bind to the Cx43 promoter at a conserved site *in vivo*, and antagonize promoter activation by Nkx2-5 and Tbx5.

Overall, the research completed for this thesis identified a novel role for Irx3 as a new

transcriptional regulator important for specialization of the cardiac His-Purkinje system. We conducted an in-depth analysis of this *Iroquois* gene family member, and demonstrated its importance in ventricular activation. Irx3 acts to precisely regulate intercellular coupling and impulse propagation, suggesting that it could be an important candidate gene for congenital or acquired conduction system diseases.

VI. Figures

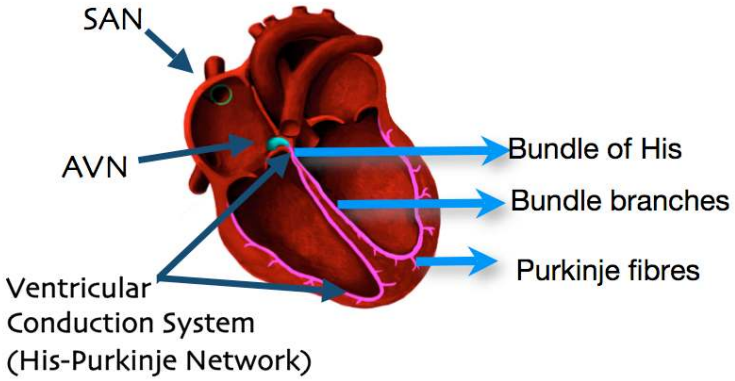

Figure 1. The mammalian cardiac conduction system (CCS).

Figure 1. The Mammalian Cardiac Conduction System (CCS).

The CCS is comprised of the peacemaking sinoatrial node (SAN), the impulse delaying atrioventricular node (AVN), and the fast conducting ventricular conduction system (VCS, or the His-Purkinje network). The VCS is further subdivided into the common bundle of His (or atrioventricular bundle), the bifurcating bundle branches, and an intricate network of subendocardial Purkinje fibers.

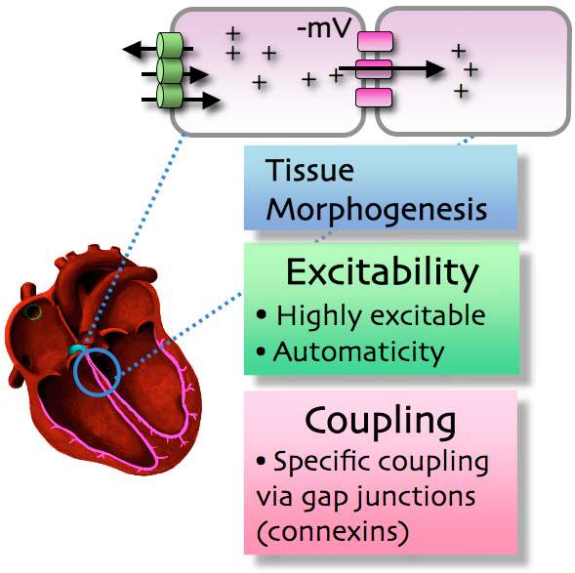

Figure 2. Determinants of impulse conduction efficiency.
(Rudy and Shaw 1997)

Figure 2. Determinants of impulse conduction efficiency.

Efficiency of impulse conduction in the VCS is largely dependent on cell and tissue morphology, cellular excitability, and intercellular coupling. VCS cells are highly excitable and couple to each other via gap junctions containing a specific set of connexins.

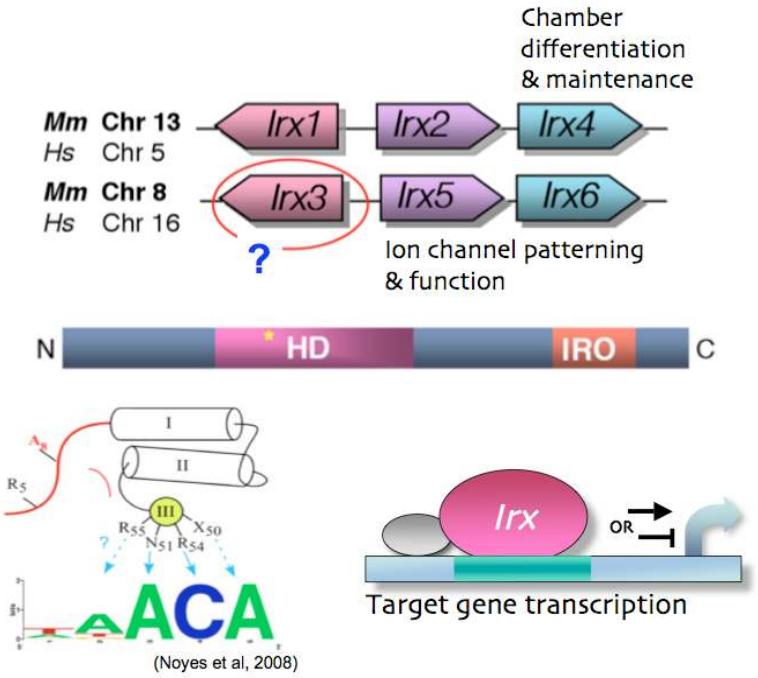

Figure 3. The *Iroquois* family of transcription factors.
(Gomez-Skarmeta and Modolell 2002) (Noyes et al., 2008)

Figure 3. The *Iroquois* family of transcription factors.

Iroquois genes are chromosomally clustered, and share a common homeobox DNA binding domain (HD) and IRO motif. Irx factors recognize a monomeric taACA consensus sequence, and can activate or repress gene transcription depending on the cellular context. In the heart, Irx4 was shown to be important for ventricular chamber differentiation. A role for Irx5 in regulating ventricular repolarization and ion channel expression patterning was also identified. *Mm*, *Mouse musculus*; *Hm*, *Homo sapiens*; HD, homeobox domain; IRO, IRO domain.

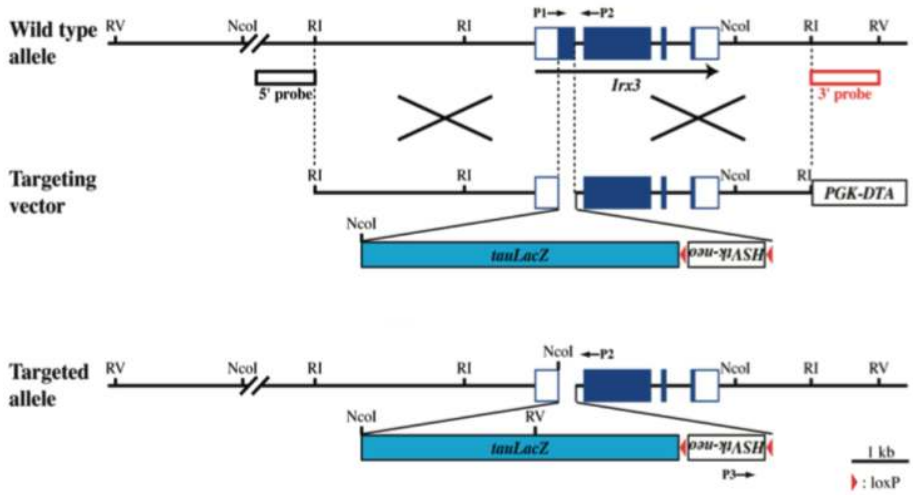

Figure 4. Gene targeting strategy for generating Irx3tauLacZ mice.

Figure 4. Gene targeting Strategy for Generating Irx3tauLacZ mice.

A loss-of-function mutation in *Irx3* was made in ES cells by replacing part of exon 1 with sequences encoding the tauLacZ reporter, immediately after the start codon. Locations for genotyping primers: P1, P2, P3 as well as 5' and 3' Southern probes are shown.

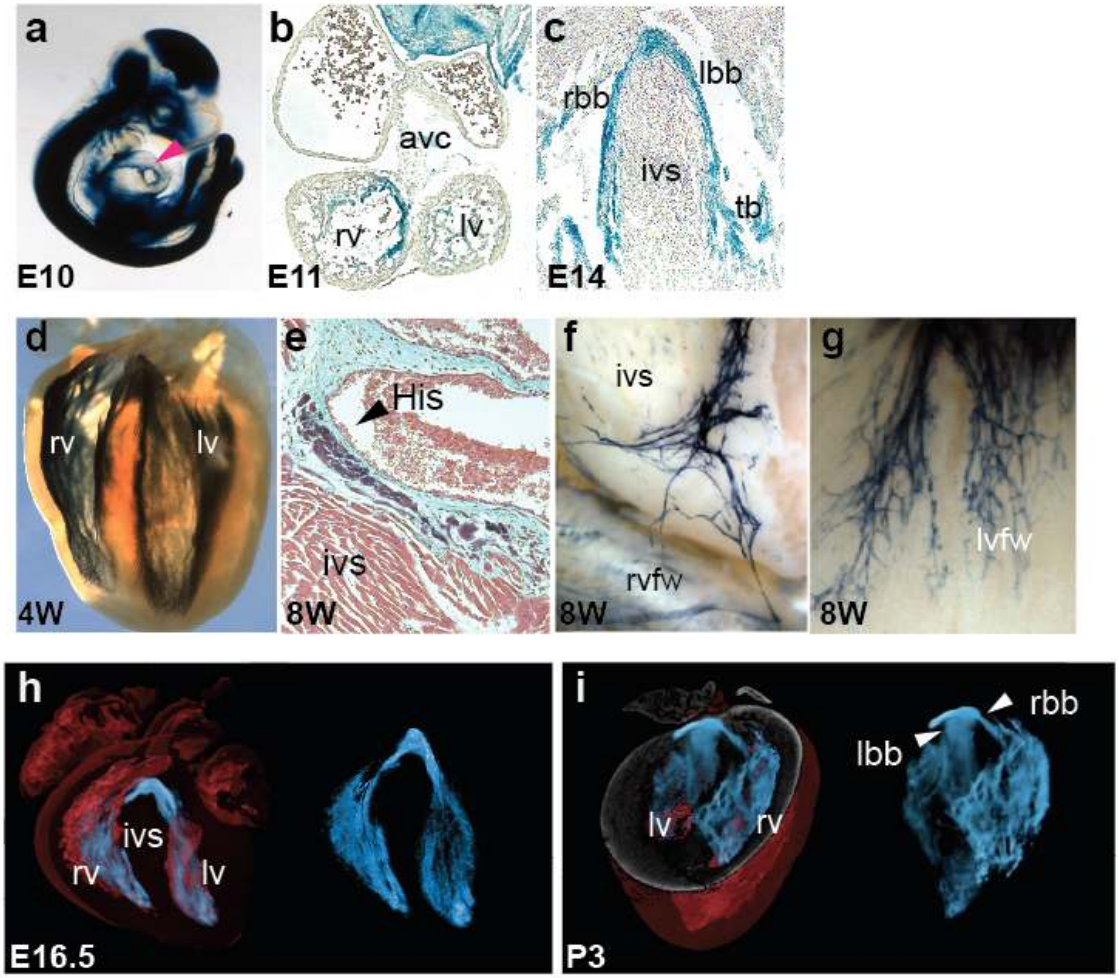

Figure 5. Irx3 is highly expressed in the developing and mature His-Purkinje network.

Figure 5. Irx3 is highly expressed in the developing and mature His-Purkinje network.

a, β-Galactosidase staining of *Irx3*$^{tauLacZ/+}$ embryos at embryonic day 10 (E10) reveals that the Irx3tauLacZ reporter recapitulates endogenous *Irx3* expression in the central nervous system. A ring-like group of cells is detected in the developing ventricle (arrowhead). **b,** Irx3tauLacZ is expressed in the developing trabeculae and in cells surrounding the developing IVS at E11. **c,** Marked cells are found in the developing bundle branches at E14. **d,** Whole-mount LacZ staining shows that Irx3tauLacZ is expressed in the His-Purkinje system at 4 weeks (4W) . **e**, Masson's trichrome staining reveals fibrous insulation of the Irx3tauLacZ^{+} bundle of His at 8 weeks (8W). **f**, Irx3tauLacZ^{+} right bundle branches extend along the septum toward the right ventricular free wall (rvfw). **g**, Irx3tauLacZ^{+} Purkinje fibers in the left ventricular free wall (lvfw) are shown. **h,** Optical projection tomography (OPT) images of Irx3tauLacZ expression in the VCS primordium at E16.5. **i,** OPT imaging shows that Irx3tauLacZ^{+} cells mature to form a highly asymmetrical His-Purkinje system by postnatal day 3 (P3). avc, atrioventricular canal; rv, right ventricle; lv, left ventricle; rbb, right bundle branch; lbb, left bundle branch; ivs, interventricular septum; tb, trabeculae; rvfw, right ventricular free wall; His, bundle of His.

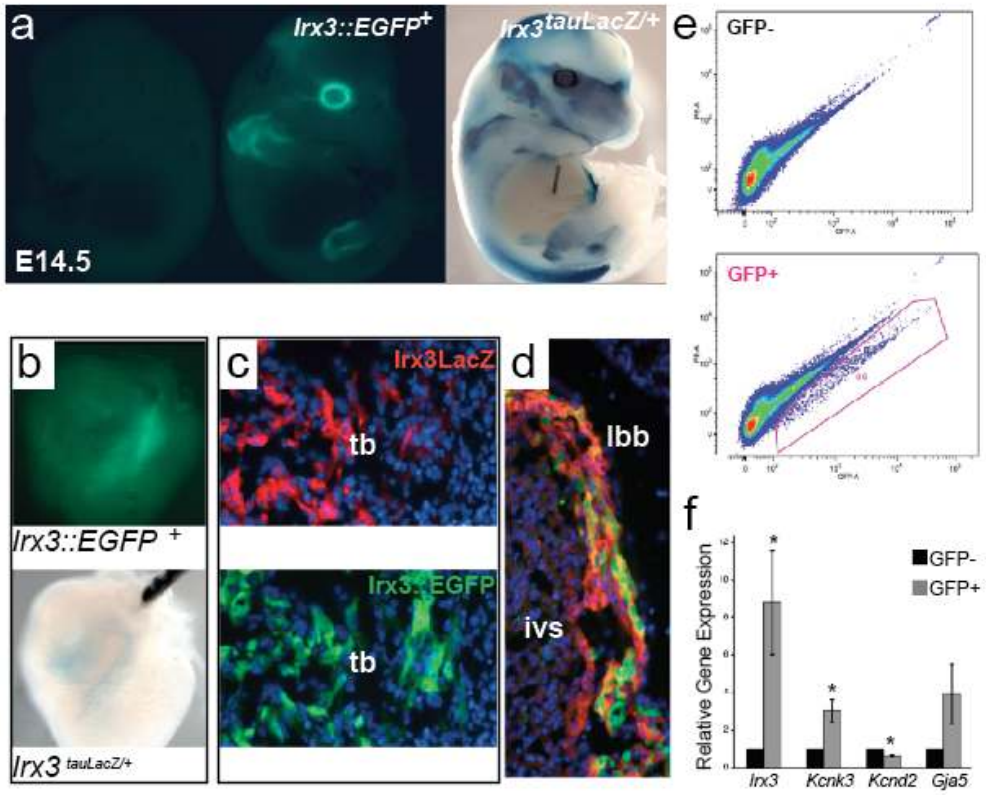

Figure 6. Characterization of the Irx3::EGFP BAC reporter.

Figure 6. Characterization of the Irx3::EGFP BAC reporter.

a, Comparison of whole-embryo expression of the Irx3::EGFP and Irx3LacZ reporters reveal their similar expression patterns in the brain, eyes, and limbs at E14.5. **b**, Both reporters are found in the developing heart. **c-d**, Immunofluorescence detection of LacZ (red) and GFP (green) in mice heterozygous for both reporters confirms their coexpression in the developing VCS. **e**, FACS sorting was used to obtain live Irx3::EGFP^{+} cells. **f**, Sorted Irx3::EGFP+ cells are enriched in VCS markers such as *Kcnk3* (minK) and *Gja5* (Cx40), but not in the epicardially enriched *Kcnd3* (Kv4.2) (normalized by GAPDH). n = 4,*, $p < 0.05$ vs. GFP-negative population. tb, trabeculae; ivs, interventricular septum; lbb, left bundle branch.

CHAPTER 1

Irx3 is Highly Expressed in Specialized Conduction Myocytes of the His-Purkinje System.

I. Background

During embryogenesis, cells of the VCS primordium are specified, instructed to develop under a specific differentiation program, and become enriched in a unique set of gene products important for their electrophysiological maturation (Boukens et al. 2009). Studies to date show that VCS cells are derived from the myocyte lineage through differentiation from a specified pool, and via paracrine induction of working myocytes by endothelial cells (Mikawa and Hurtado 2007). However, others have suggested that conduction system myocytes could be derived from other cell types of the developing heart, such as those of the migrating neural crest (Gittenberger-de Groot et al. 2003; Nakamura et al. 2006).

During early heart development, a ring-like population of subendocardial myocytes between the future right and left ventricles, along with cells atop the growing interventricular septum, and a subset of the proliferating trabeculae, form the initial primordial framework from which the future His-Purkinje system develops (Viragh and Challice 1982). Differentiation of this cell population continues between E11 and E14 in the mouse, during which time an apex-to-base contraction sequence evolves from a simple linear activation pattern (Morley and Vaidya 2001). As they differentiate, conduction myocytes exit the cell cycle between E12 and E14 (Sedmera et al. 2003a). Shortly after, VCS cells start to show specific expression of markers such as enrichment of the gap junction gene connexin 40 (Cx40) throughout the conduction axis, and

downregulation of Cx43 in the proximal bundle branches (Delorme et al. 1997). The mature His-Purkinje network is eventually attained through further differentiation of the initial framework and neonatal remodeling (Meysen et al. 2007; Mikawa and Hurtado 2007).

Cells of the VCS have the ability to spontaneously generate an action potential, and differ in their ability to propagate action potentials in comparison to working myocytes (Schram et al. 2002). These characteristics are determined by the specific expression of ion channels, and include the progressive enrichment of genes such as Scn5a, Scn1b, and Hcn4 during development (Boukens et al. 2009; Remme et al. 2009; Aanhaanen et al. 2010). The underlying intrinsic molecular signals accompanying VCS functional maturation remains an active area of investigation.

II. Results and Discussion

Lineage analysis at E14.5 revealed that Irx3tauLacZ$^+$ cells, with the exception of those marking the distal VCS in the left ventricle, are predominantly derived from the *Mef2CAHF::Cre/ROSA-YFP*-labeled ventricular myocyte lineage (Figure 7a-a') (Verzi et al. 2005). This finding is consistent with studies demonstrating that conduction system cells are derived from the myocyte lineage (Cheng et al. 1999), and suggests that VCS precursor cells could reside in the first and second heart fields. Cardiac neural crest cells, which have been shown to migrate into the heart to participate in outflow tract development and maturation of the VCS (St Amand et al. 2006), have been suggested to differentiate into conduction myocytes (Nakamura et al. 2006). However, our lineage tracing studies show that while Irx3tauLacZ$^+$ cells are closely associated with neural crest

derived cells, marked by *Wnt1-Cre*/*ROSA-YFP,* they do not co-express LacZ and YFP (Figure 7b-b') (Danielian et al. 1998). This shows that although neural crest-derived are within close proximity to the VCS, and could participate in its functional maturation, they do not become incorporated in the conduction system tissue.

Gene expression analysis in the developing heart shows that Irx3tauLacZ^{+} cells are subendocardial myocytes that express VCS markers. In neonatal hearts, Irx3tauLacZ^{+} cells express Scn5a and Hcn4, both of which encode ion channel subunits that become progressively enriched in the ventricular conduction system (Figure 8a,b). At E14.5, Irx3tauLacZ^{+} cells, which are surrounded by endocardial cells marked by platelet/endothelial cell adhesion molecule-1 (PECAM), also express the myocyte-specific actin-binding protein, tropomyosin (Figure 8c-d'). Tropomyosin was also found in cultured neonatal ventricular working myocytes, including those marked by Irx3::EGFP (Figure 8e). These data demonstrate that developing Irx3-expressing cells are indeed subendocardial myocytes of the VCS.

In neonatal and 8-week old adult mice, cells that express Irx3tauLacZ at high levels also express the VCS-specific gap junction protein Cx40. Colocalization of LacZ and GFP was detected in the maturing bundle branches and Purkinje fibers of $Irx3^{tauLacZ/+};Cx40^{EGFP/+}$ neonatal mice (Figure 9a). In adult hearts, co-localization was found in the conduction tissue, but not in underlying coronary arteries which are also known to express Cx40 (Figure 9b). Adult Irx3tauLacZ^{+} bundle branch cells expressed Cx40 at cell borders; wherein Cx40^{+} plaques were detected at longitudinal ends of the cell (Figure 8 c). These findings demonstrate that Irx3 is highly enriched in the specialized myocytes of the ventricular conduction system.

We sought to determine if cells expressing Irx3 exhibit enhanced automaticity and show connexin expression patterns that are characteristic of VCS myocytes. Fluorescence from Irx3::EGFP transgenic reporter mice (Figure 5) was used to identify Irx3-expressing myocytes isolated from the proximal VCS at E14.5. Calcium imaging of reaggregated cells show that Irx3::EGFP^{+} myocytes indeed have higher automaticity than non-GFP cells, and can drive depolarization of non-fluorescent neighboring cells (Figure 10a). In agreement with the gradual enrichment of Cx40 to conduction myocytes of the proximal VCS and down regulation of Cx43 in these cells during development (Delorme et al. 1997), quantitation of cell pairs for clear Cx plaque expression show that the majority of cells isolated from the proximal VCS (Irx3::EGFP^{+}) express Cx40 at cell-cell borders (Figure 10b,c). In contrast, the majority of non-GFP myocytes cells are enriched in Cx43 plaques at cell-cell borders. These specific properties of Irx3-expressing cells are consistent with that of specialized VCS myocytes.

III. Figures

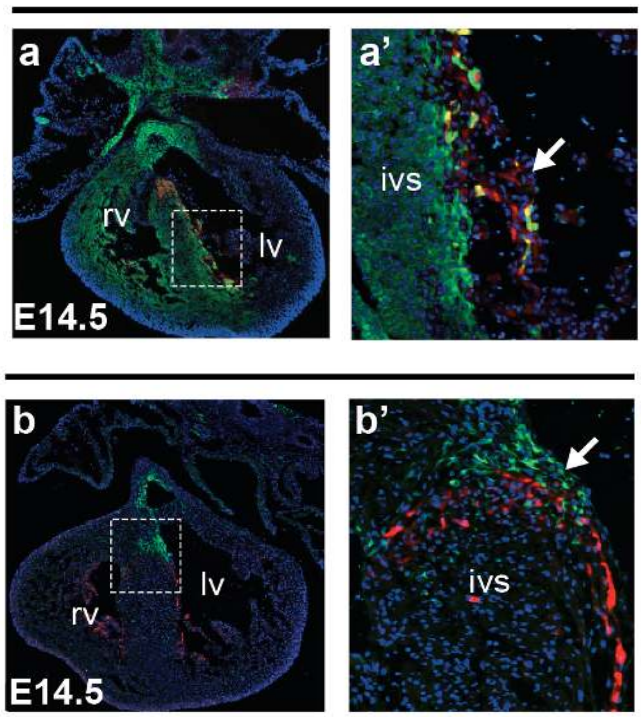

Figure 7. Irx3^{+} cells are predominantly derived from ventricular myocyte precursors and not from cells of the neural crest.

Figure 7. Irx3^{+} cells are predominantly derived from ventricular myocyte precursors and not from cells of the migrating neural crest.

a-a', Lineage analysis in mice expressing Irx3tauLacZ^{+} VCS cells (red) show that they are predominantly derived from the *Mef2CAHF::Cre/ROSA-YFP*-labeled ventricular myocyte lineage, with the exception of some cells of the developing distal VCS in the left ventricle (arrow). **b-b',** Lineage analysis in mice expressing Irx3tauLacZ^{+} (red) and *Wnt1-Cre/ROSA-YFP* (green) show that Cre-labeled neural crest-derived cells are closely associate with the VCS, but do not make direct contributions to the conduction tissue.

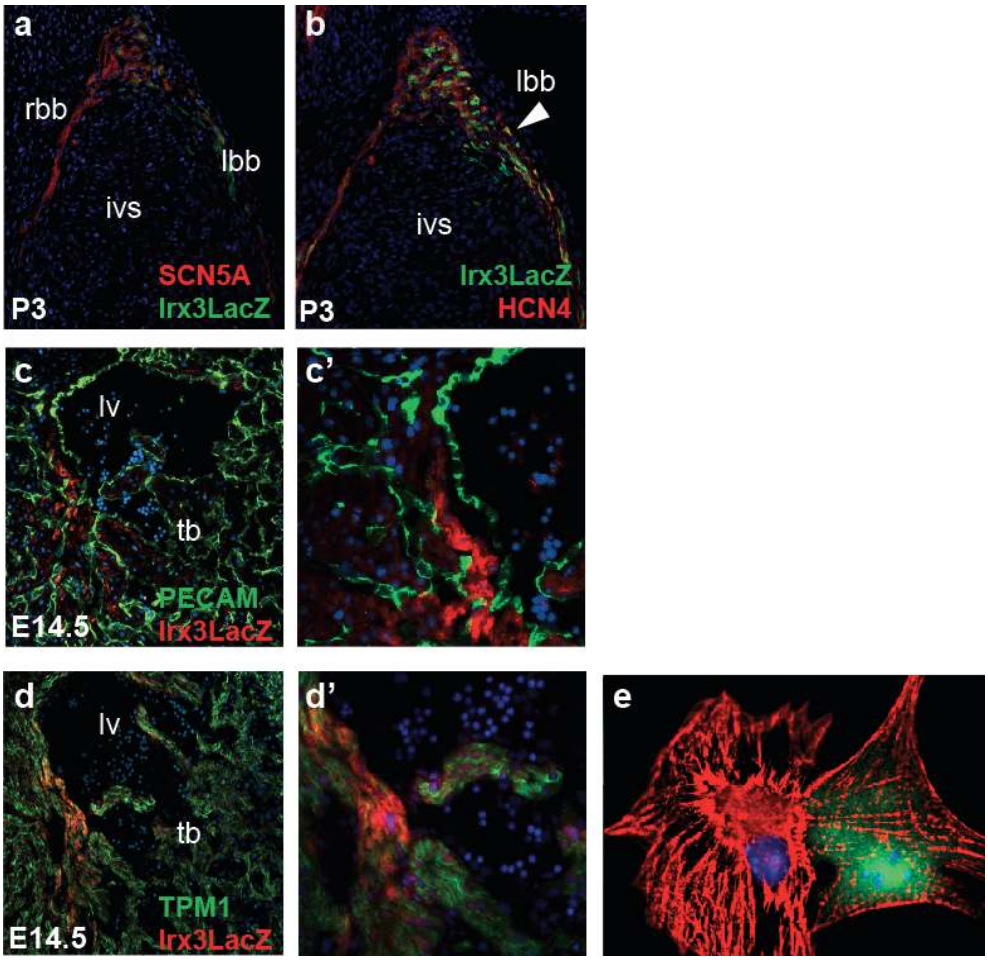

Figure 8. Irx3tauLacZ^{+} cells are subendocardial myocytes that express VCS markers during development.

Figure 8. Irx3tauLacZ^{+} cells are subendocardial myocytes that express VCS markers during development.

a, Immunofluorescence colocalization shows that Irx3tauLacZ^{+} (green) cells express Scn5a (red) in the proximal VCS at P3. **b**, Irx3tauLacZ and Hcn4 are coexpressed in the proximal VCS at P3. **c-c'**, Irx3tauLacZ^{+} cells are surrounded by PECAM^{+} cells of the developing endocardium. **d-d'**, Immunofluorescence colocalization shows that Irx3tauLacZ^{+} cells coexpress tropomyosin 1 (TMP1) at E14.5. **e**, At P3, TMP1 is expressed in neonatal ventricular myocytes as well as conduction myocytes marked by Irx3::EGFP (green).

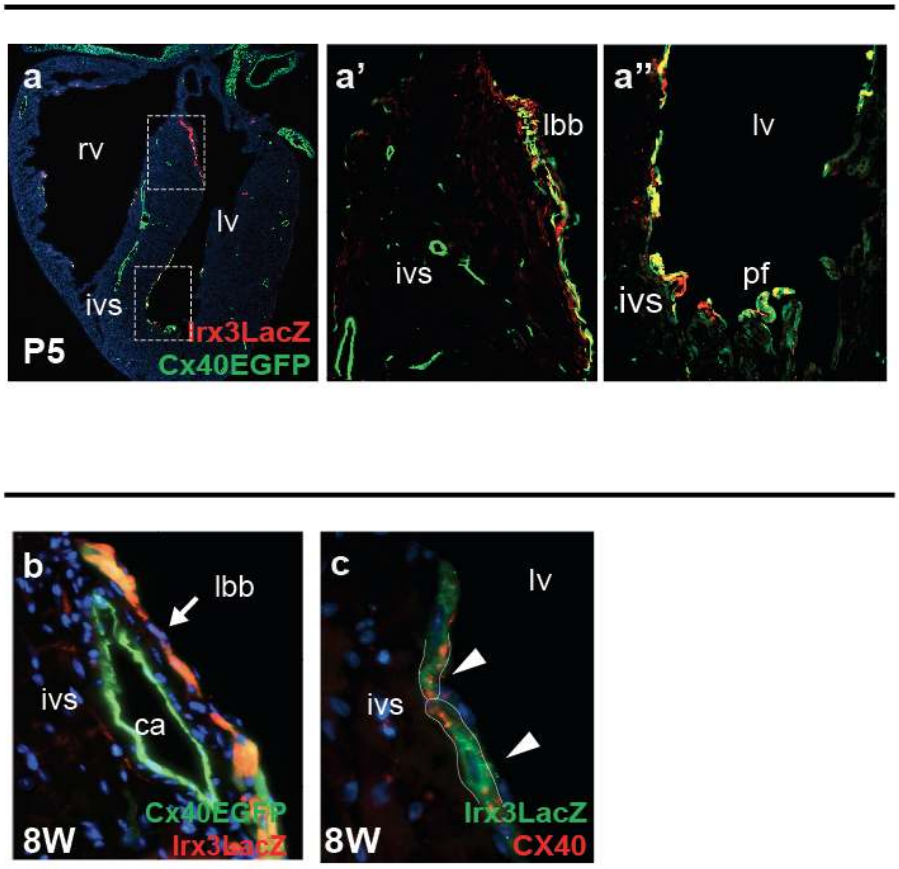

Figure 9. Irx3tauLacZ^{+} cells coexpress the VCS-specific marker Cx40 in developing and adult hearts.

Figure 9. Irx3tauLacZ^{+} cells coexpress the VCS-specific marker Cx40 in developing and adult hearts.

a, Colocalization of Irx3tauLacZ and Cx40EGFP in the VCS of *Irx3$^{tauLacZ/+}$;Cx40$^{EGFP/+}$* mice at P5. High levels of coexpression are detected in the bundle branches (**a'**) and Purkinje fibers (**a''**). **b,** Irx3tauLacZ is coexpressed with Cx40EGFP in the adult VCS but not in coronary arteries (ca). **c**, Adult Irx3tauLacZ^{+} bundle branch cells express Cx40 at longitudinal cell borders. lbb, left bundle branch; ivs, interventricular septum; pf, Purkinje fiber; lv, left ventricle; ca, coronary artery.

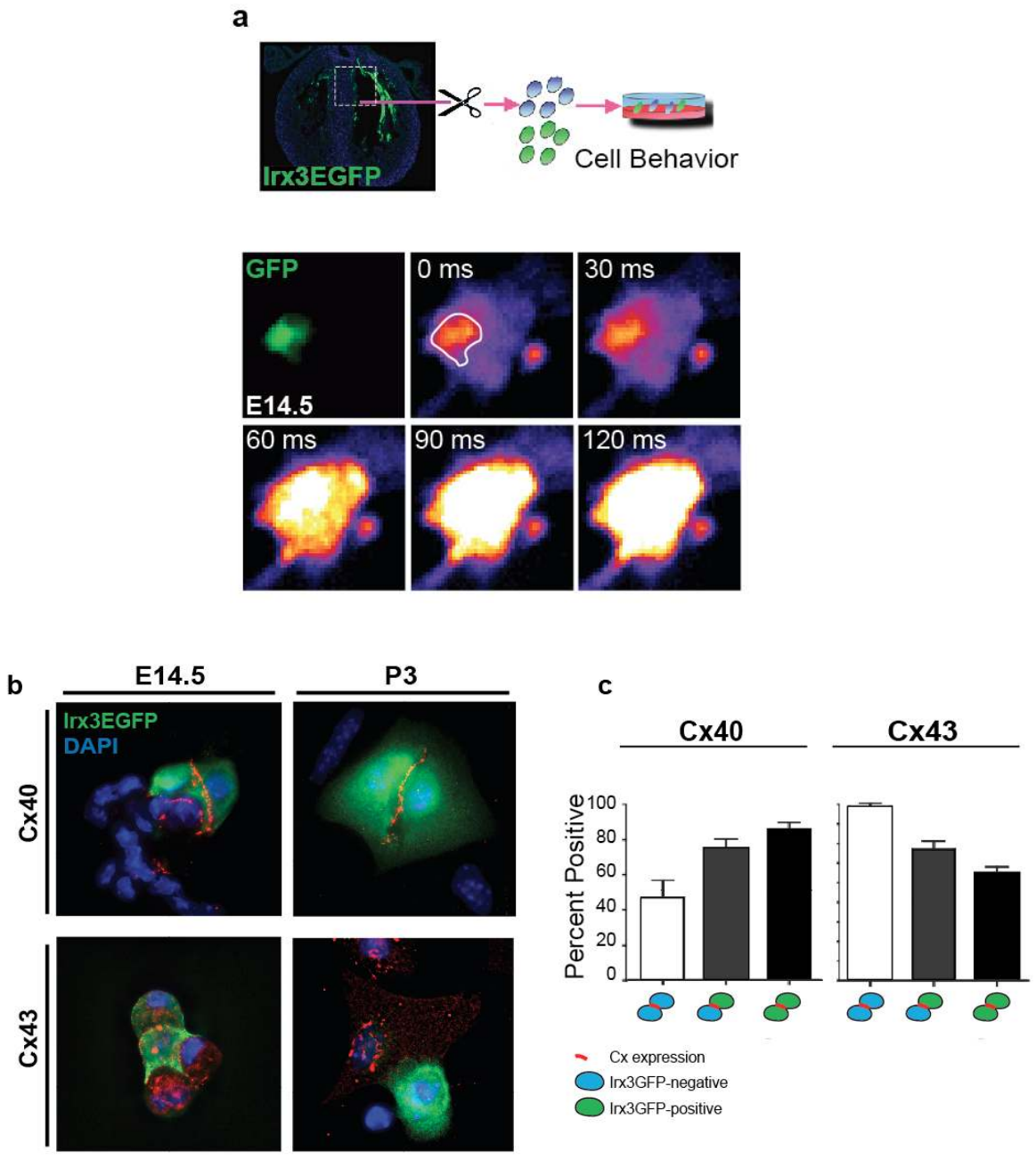

Figure 10. Irx3-expressing cells have higher automaticity than non-GFP working myocytes and preferentially express Cx40 at cell borders.

Figure 10. Irx3-expressing cells have higher automaticity than non-GFP working myocytes and preferentially express Cx40 at cell borders.

a, Calcium flux imaging of reaggregated cells from the proximal VCS shows that Irx3::EGFP^{+} cells exhibit higher automaticity than non-GFP working myocytes by driving the depolarization of neighboring non-GFP cells (at E14.5). **b**, Reaggregated cells, isolated from the proximal VCS, show progressive enrichment of Cx40 to cell borders of Irx3::EGFP^{+} conduction system myocytes (at E14.5 and P3). In contrast, Cx43 expression is enriched in non-GFP working myocytes. **c**, Quantitation of cell pairs for clear Cx plaque expression show that the majority of cells isolated from the proximal VCS (marked by Irx3::EGFP, green cell pairs) expresses Cx40 at cell borders. In contrast, the majority of non-VCS cells (non-GFP cell pairs) express Cx43 at cell borders.

CHAPTER 2

Loss of *Irx3* Leads to Abnormal Electrical Activation of the Ventricles

I. Background

The overall sequence of electrical activation of the heart from atrial depolarization to ventricular repolarization can be measured and recorded with various electrophysiology (EP) techniques that have been adapted for the mouse (Gehrmann and Berul 2000). Whether loss of Irx3 could affect the spread of conduction in the heart was assessed by EP approaches that include surface electrocardiography (ECG), intracardiac ECG, and optical activation mapping. A brief background on these methods and how they pertain the observed loss-of-function phenotype is provided in this section.

ECG is a method of recording the spread of electrical currents generated by the heart within each cardiac cycle over time, and can be obtained using multiple leads on the body's surface (Guyton and Hall, 2005). This is possible because a small portion of the current generated by the heart spreads through surrounding tissue all the way to the body surface. Electrical voltages generated within each cardiac cycle are represented as P, Q, R, S, and T deflections (Figure 11a). Using lead II as an example (reference electrode on the right arm and exploring on the left leg), the positive P wave is caused by the spread of depolarization, measured as the projection of the instantaneous net dipole vector generated within the atrial muscle onto the lead, from the SAN toward the left atrium. The period of zero potential immediately following the P wave is due to the relatively much smaller size of the AV node through which the impulse is delayed. The projection of its small net dipole vector is not sufficient to be detectable thus resulting in a flat tracing. This period also includes the depolarizing impulse moving into the His bundle

and the Purkinje network which are also too small to create a detectable net dipole. The length of time between the start of the P wave and the end of the period of zero potential is known as the P-R interval which is a measure of the effectiveness of the AVN in delaying ventricular activation.

The subsequent negative deflection of the Q wave is due to movement of depolarization through the left bundle branch into the interventricular septum (IVS) from left to right, creating a net dipole pointing away from the exploring electrode. As the impulse begins to move out of the Purkinje network and into the right and left ventricular muscles, there are dipoles pointing in both directions. Since the left ventricular chamber is much larger in size, the instantaneous net dipole vectors end up pointing downward and to the left. Consequently, a positive deflection of the R wave is detected and becomes even more positive when the right side of the heart finishes depolarizing first. The mouse ventricle was shown to also depolarize in a baso-apical fashion (Jongsma and Wilders 2000). This activation sequence was carefully measured by activation mapping and attributed to a direct continuity of cells found at the bottom of the common His bundle with working myocytes atop the IVS.

The negative S wave that follows is due to the upward depolarization vector of the left ventricular base away from the exploring electrode. The subsequent period of zero potential, the ST segment, occurs when both ventricles are completely depolarized, and corresponds to the plateau phase of the ventricular action potential when calcium entry is causing myocytes to contract. However, no ST segment can be distinguished in the mouse as the T wave emerges with the end of the QRS complex. Lastly, since subendocardial cells have longer action potential durations than subepicardial cells,

repolarization takes place from the epicardium to the endocardium. In humans, this rightward repolarization is detected as the positive T wave deflection.

Although ECG measurements do not show electrical activities of the SAN, AVN, and His-Purkinje network due to their relatively small tissue size, the QRS complex can be used as an indicator of the effectiveness of the Purkinje network. A prolonged QRS suggests that the depolarization is moving by a slower route through the ventricular muscle and may result from a block in the branching fibers. Rapid shifts in voltages and axis deviations, as a result of irregular impulse conduction, can be caused by multiple small local blocks in the Purkinje fibers. This often causes additional peaks of the QRS complex (i.e. RsR' complex in lead I), which was observed in loss of function mutations of Id2, Tbx5, and Nkx2.5 (Moskowitz et al. 2007).

When His-Purkinje function is compromised, the cardiac impulse can be slowed or even blocked along the pathway. This would decrease the velocity and pattern of impulse conduction through the ventricular chambers. In open-chest ventilated mice, effectiveness of ventricular activation can be measured by following the timing of impulse propagation between two recording electrodes. This intracardiac ECG method can be used to determine conduction time between the atria, the His bundle, and the ventricle (AV, AH, HV intervals). Potential abnormal His bundle function in Irx3 mutants could be detectable as a prolongation of the HV interval (His bundle-to-ventricle). Briefly, a catheter is placed through the right jugular vein and the right atrium to the right ventricle. While distal electrodes pace and record from the right ventricle, proximal electrodes pace and record from the right atrium. Middle electrode pairs can also be used to record distinct triphasic His bundle electrograms (Gehrmann and Berul

2000; Maguire et al. 2000).

Propagation measurements in the methods introduced thus far assume that the wavefront travels in a straight line between electrodes. However, the heart is a three-dimensional structure with anisotropic conduction. Optical mapping is a more precise method which takes into account how a pathway of conduction affects the surrounding tissue (Rosenbaum and Jalife, 2001). It has been used to obtain high resolution spatial and temporal mapping of epicardial conduction patterns and velocities of the isolated perfused mouse heart (Morley et al. 2000; Morley and Vaidya 2001). After staining with voltage-sensitive dyes such as di-4-ANEPPS (binds to the plasma membrane and changes its spectroscopic properties linearly in accordance with changes in membrane potential), florescence signals from the traveling excitations over a period of milliseconds are recorded by a charge-coupled device (CCD) camera.

Although the zebrafish heart is comprised of a single atrial chamber and a single ventricular chamber, it activates in a controlled apex-to-base fashion similar to mammalian hearts (Chi et al. 2008). Although histologically defined tracts of specialized conduction cells have not yet been described within the fish ventricle, studies have identified bands of trabeculae that are continuous with the atrioventricular canal and ventricular apex (Sedmera et al. 2003b). These cells are thought to serve as a functional equivalent of the His-Purkinje system. Zebrafish conduction system function has been successfully studied by optical mapping of live animals expressing the calcium reporter *Tg*(*cmlc2*:*gCaMP*)^{s878} (Chi et al. 2008)

Using these invaluable tools and techniques, a growing number of VCS-specific genes continue to be discovered and investigated for their functional significance in heart

conduction. Given the highly enriched expression of Irx3 in the His-Purkinje network, and previous studies which showed that Irx5 is critical for ventricular repolarization (Costantini et al. 2005), we asked whether and how genetic ablation of Irx3 could impact heart function and impulse spread.

II. Results and Discussion

We examined the phenotype of *Irx3*$^{taulacZ/tauLacZ}$ mice and found that they are viable, fertile and do not manifest abnormalities in heart morphology, size, or contractile function when assessed by echocardiography (data not shown). However, by 2 weeks of age, these mice exhibited ventricular activation defects when assessed by surface ECG (Figure 11). The phenotype was characterized by prolonged QRS interval durations and notched R waves (R'), both of which are indicative of delays in ventricular activation. QRS prolongation and notched R' waves were also observed in freely moving mice by telemetry ECG analysis. Note that PR and QTc intervals, which reflect atrioventricular delay, and ventricular repolarization respectively, were unaltered in mice lacking Irx3 (Figure 12a). These results are expected since Irx3 is not normally expressed in the regions that these last two ECG parameters reflect.

Right axis deviation, detectable as a negative QRS deflection in lead I combined with a positive deflection in Lead II, was observed in the majority of Irx3 null mice (Figure 11). These observations point to bundle branch block, and/or abnormal impulse conduction in the right ventricular free wall, as mechanisms underlying the observed phenotype. In the absence of abnormal heart orientation or structural changes, these

results suggest that the conduction defect is likely specific to the conduction system tissue (Castellanos et al. 1970), where Irx3 is normally highly expressed.

Indeed, intracardiac ECG recordings revealed that while impulse spread from the atria to the His bundle (AH interval) was unaffected by the loss of Irx3 (Figure 12d), there was a significant increase in conduction time between the His bundle and the ventricles (HV interval) (Fig. 12b,c). These results point to conduction slowing or block within this conduction pathway.

Optical mapping of epicardial activation revealed abnormal activation of the ventricles (Fig. 13a). Normal activation of both ventricles through the right and left bundle branches is manifested as two breakthrough points reflecting synchronous activation of both sides (Nygren et al. 2000). However, the majority (77%) of Irx3 null hearts had a single breakthrough from the left ventricular apex, along with significantly slowed conduction velocity (Figure 13b), thus establishing that activation phenotype is characterized by right bundle branch block (RBBB). Although the entire VCS is devoid of Irx3, the manifestation of conduction block in the right side of the heart is not unexpected, and is similar to the phenotype of mice lacking Cx40 throughout the ventricular conduction system tissue (Tamaddon et al. 2000). This could be explained by the lower safety factor for conduction expected for the right conduction pathway (Fast and Kleber 1995a; Fast and Kleber 1995b), where constituent cells have shorter action potential durations and make up only a few thin bundle branches (1-2 bundles). In comparison, a large group of cells with longer action potential durations comprise the left pathway (~20 bundles) (Myerburg 1971; Miquerol et al. 2004).

To examine whether right bundle branch block is caused by conduction slowing, or by a complete block, our collaborators measured conduction velocity in the VCS in mice expressing the $Cx40^{EGFP}$ reporter. $Irx3^{taulacZ/taulacZ}$;$Cx40^{EGFP/+}$ mice showed significantly diminished conduction velocity through the fibers as compared to $Cx40^{EGFP/+}$ mice (Figure 13c). These results indicate that observed abnormal ventricular activation pattern is due to conduction slowing in cells lacking Irx3.

Finally, to address if Irx3 function is evolutionarily conserved, we examined its role in zebrafish, where the z*iro3a* ortholog, but not the more divergent *ziro3b*, is expressed in the heart at 48 hours post fertilization (Figure 14a,b). Optical mapping was performed by our collaborators in live zebrafish expressing the *in vivo* calcium transient reporter $Tg(cmlc2{:}gCaMP)^{s878}$ (Chi et al. 2008). Similar to our observations in mice, inhibition of *ziro3a* by morpholino antisense oligonucleotides caused slowed and abnormal impulse conduction in the ventricle (Figure 4c). These data uncover an evolutionarily conserved role for Irx3 in regulating ventricular activation.

In summary, we undertook a variety of whole heart and animal electrophysiology approaches to show that loss of *Irx3* results in abnormal ventricular activation. In mice, the conduction defect was characterized by right bundle branch block. We also found that the closely related *ziro3a* homolog is highly enriched in the fish ventricle and required for normal ventricular activation function.

III. Figures

a

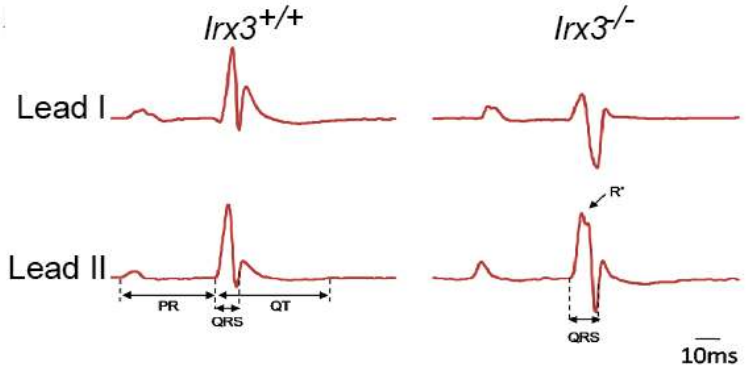

b

	Postnatal Day 14		8 Weeks		
	QRS (ms)	R' (%)	Telemetry QRS (ms)	QRS (ms)	R' (%)
Irx3$^{+/+}$	10.2 ± 0.2	0	10.4 ± 0.5	9.9 ± 0.2	0
Irx3$^{-/-}$	13.5* ± 0.3	67	14.2* ± 0.9	12.2* ± 0.5	83

Figure 11. Loss of Irx3 leads to QRS prolongation and RsR' wavefronts.

Figure 11. Loss of Irx3 leads to QRS prolongation and RsR' wavefronts.

a, Representative 6-lead surface ECG tracing in leads I and II shows prolongation of the QRS interval and abnormal R' wave in Irx3 null mice. **b,** A summary of 6-lead, and telemetry ECG parameters. Ventricular activation defects were measurable as early as 2 weeks of age. n = 8-12; *, $p < 0.05$ versus wildtype.

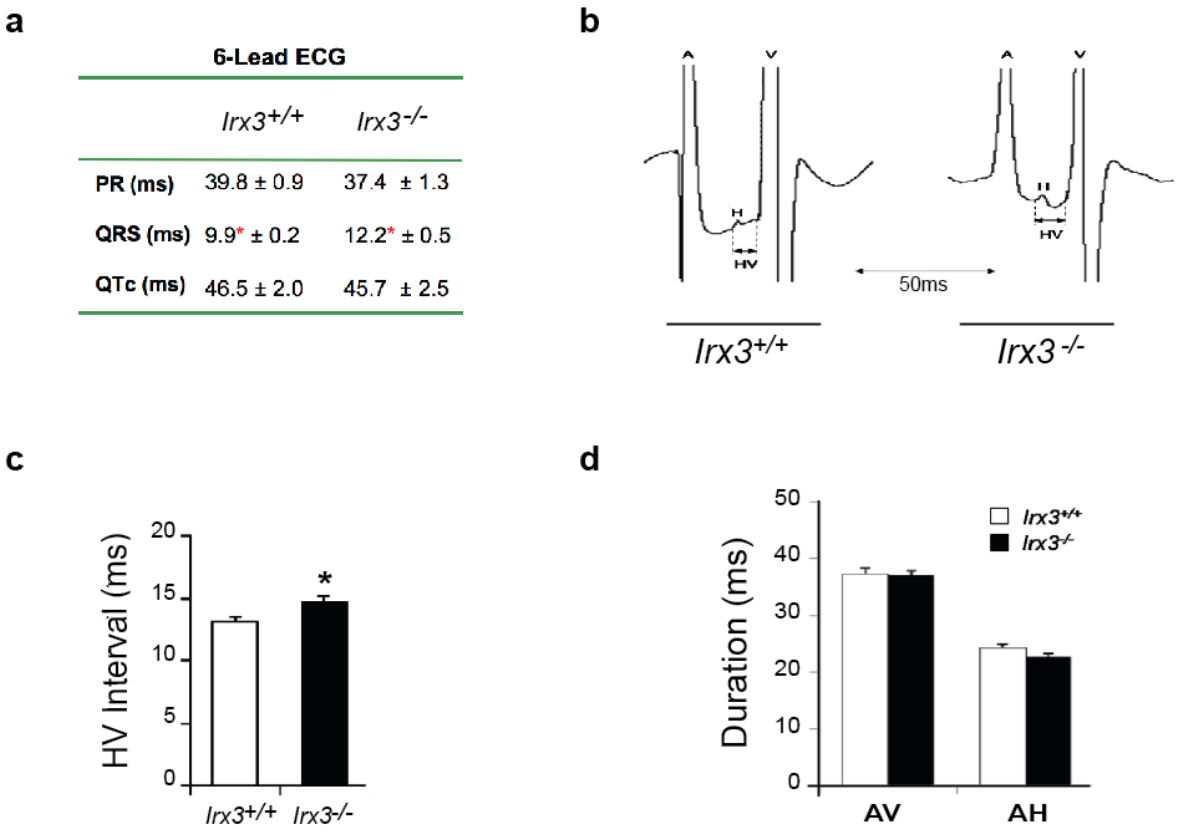

Figure 12. Loss of Irx3 leads to abnormal ventricular activation.

Figure 12. Loss of Irx3 leads to abnormal ventricular activation.

a, A summary of surface ECG parameters showing that PR and QTc conduction times were not significantly different between genotypes. **b**, Representative octapolar intracardiac ECG traces illustrating atrial, ventricular, and His-bundle depolarization signals show prolongation of HV conduction time in mice lacking Irx3. **c,** Quantification of intracardiac ECG parameters revealed significantly prolonged HV conduction times in mice lacking Irx3. $n = 9$; *, $p < 0.05$ vs. wildtype. **d**, Consistent with the absence of Irx3 expression in the atria or AV node, AV and HV conduction times are unchanged.

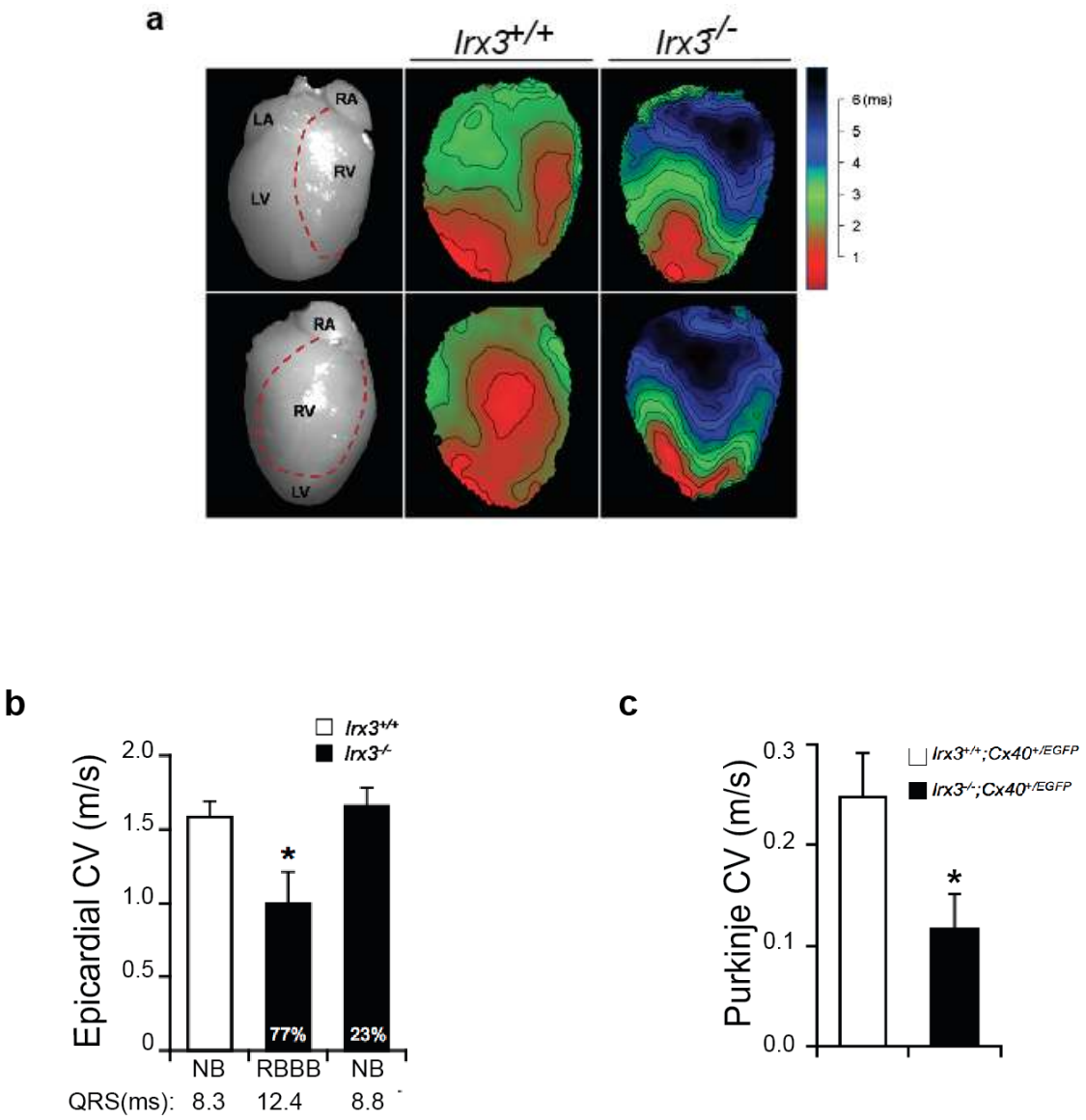

Figure 13. Loss of Irx3 leads to abnormal ventricular activation characterized by right bundle branch block.

Figure 13. Loss of *Irx3* leads to abnormal ventricular activation characterized by right bundle branch block.

a, Optical mapping results are shown in apical four-chamber, and apical right ventricular two-chamber views. Representative epicardial activation maps reveal 2 breakthrough points in the apex of wildtype hearts. Irx3 null hearts lack right ventricular breakthrough, indicating conduction block along the right conduction pathway. Isochrone lines mark areas where depolarization reached 50% intensity in consecutive 0.5 ms intervals. Depolarization proceeded in an apex-to-base direction. Red indicates earliest activation time (ms). wildtype, n = 12; Irx3 null, n = 9. **b,** Quantitation of epicardial conduction velocity and corresponding QRS intervals shows that 77% of hearts lacking Irx3 had RBBB along with slowed epicardial conduction velocity (CV) and QRS widening, in comparison to wildtype hearts, and the 23% of Irx3 null hearts that did not show conduction block (NB). Values are mean ± SEM; n = 4-6; *, $p < 0.05$. **c,** Quantitation of VCS fiber conduction velocity shows slowed CV in $Irx3^{taulLacZ/tauLacZ};Cx40^{EGFP/+}$ fibers compared to those of $Irx3^{+/+};Cx40^{EGFP/+}$ mice. Values are means ± SEM, n = 6-7; *, $p < 0.05$. NB, no block; RBBB, right bundle branch block.

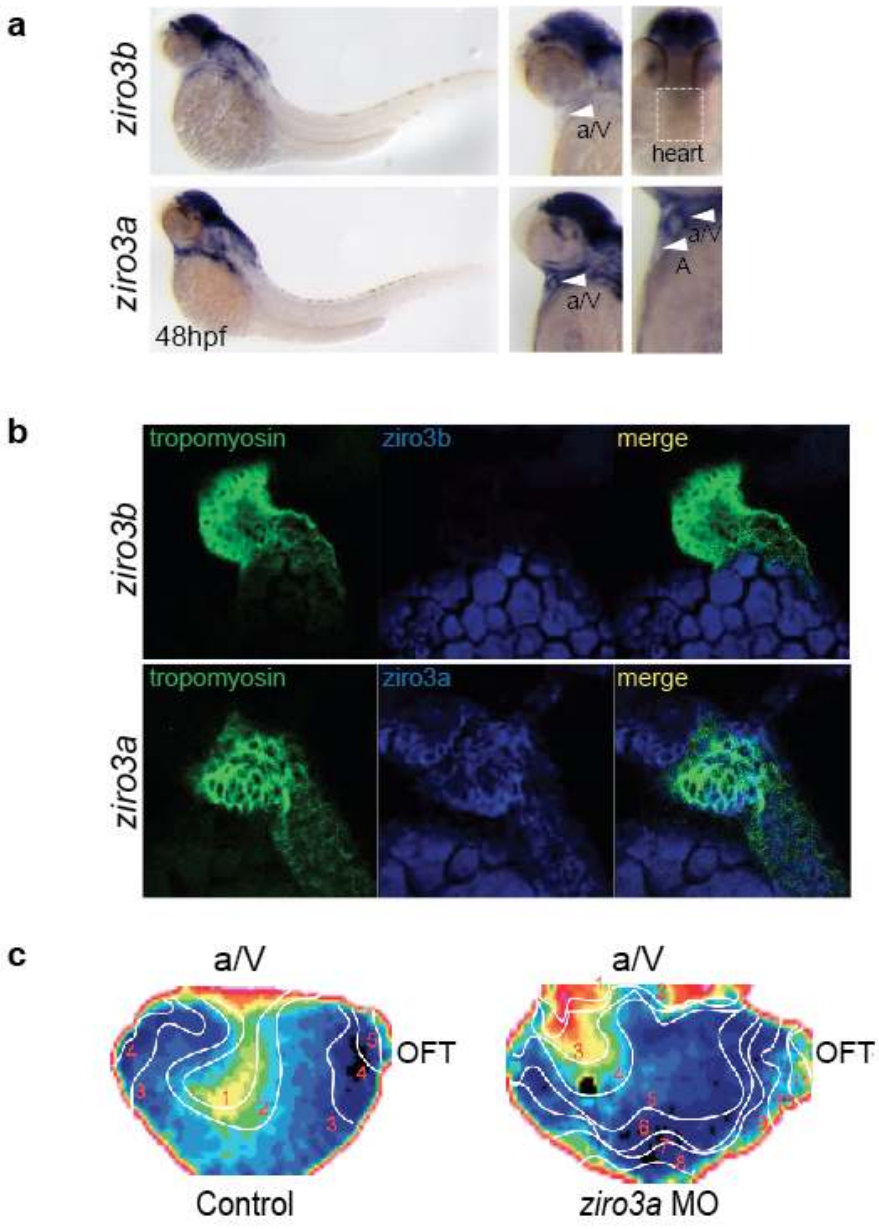

Figure 14. *Ziro3a* is required for ventricular activation in zebrafish.

Figure 14. *Ziro3a* is required for ventricular activation in zebrafish.

a, The *Irx3* ortholog *ziro3a*, but not the more divergent *ziro3b*, is expressed in the heart at 48 hours post fertilization. **b**, Fluorescence in situ hybridization shows strong colocalization of *ziro3a* and myocyte-specific tropomyosin-1 in the ventricle. **c**, Optical mapping of live zebrafish expressing the *Tg(cmlc2:gCaMP)s878* calcium reporter shows that inhibition of *ziro3a* by morpholino oligonucleotides caused abnormal impulse propagation in the ventricle. Each isochronal line represents 40ms. A, atria; V, ventricle; a/V, atrioventricular canal; OFT, outflow tract; MO, morpholino knockdown

CHAPTER 3

Irx3 regulates cellular excitability and coupling in the VCS.

I. Background

Impulse conduction efficiency depends on the interplay of several factors including tissue morphology, membrane excitability, and intercellular coupling, the latter of which has been shown by computer modeling to be an important determinant for rapid directional impulse propagation (Rudy and Shaw 1997; Rudy 1998; Rudy 2005).

Cells of the VCS have higher automaticity, a faster rate of depolarization, and longer action potential durations as compared to ventricular myocytes (Schram et al. 2002).These excitability characteristics are determined by the expression pattern, level, and kinetics of various voltage-gated ion channels. The efficiency of action potential firing is largely dependent on the inward sodium current (I_{Na}) which dictates the rate of membrane depolarization, and the ability of the cell to spontaneously reach the firing threshold (Figure 15). The latter is dependent on the I_f current which is encoded by the hyperpolarization-gated cyclic nucleotide-gated family of channels.

Gap junction channels, which reside in inter-membrane connections between cardiac cells known as intercalated disks, provide a low resistance pathway for the propagation of the action potential between adjacent cells in the heart. The density and composition of gap junctions determine cell-cell coupling efficiency and ensure orchestrated patterns of current flow (Rudy and Shaw 1997). A gap junction is formed by head-to-head docking of 2 hemichannels (connexons), each of which is made up of 6 connexins surrounding an aqueous pore (Figure 16). When 2 connexons containing the same connexin are paired, the junction formed is known as a homomeric/homotypic

connection. When each connexon containing a separate type of connexin isoform is docked, a homomeric/heterotypic junction is formed. Lastly, heteromeric/heterotypic junctions refer to those formed between 2 different connexons each containing different proportions of 2 or more connexins. Although the permeability and conductance of these possible arrangements of gap junction channels have been widely studied in cell systems, their presence and role in the heart has been difficult to confirm (Cottrell and Burt 2005).

Three connexins, Cx40, Cx43, and Cx45 are predominantly found in the His-Purkinje system (Cole et al. 1988; Saez et al. 2003). Given that the type of Cx present in a particular gap junction determines the conductance of the channel, VCS cells are selectively coupled via various combinations of the above-mentioned Cxs in specific patterns within the conduction tissue (van Veen et al. 2005). This extensive expression of connexins within His-Purkinje subdomains have been suggested to underlie fast conduction due to finely tuned electrical coupling (Kleber and Rudy 2004). Thus, changes in Cx expression levels and pattern could alter the efficiency of rapid and directional impulse spread from cell to cell.

For example, heart-specific deletion of Cx40 resulted in QRS prolongation and abnormal ventricular activation characterized by right bundle branch block (Tamaddon et al. 2000). Moreover, the proximal VCS, which consists of the common bundle of His and branching bundles near the top of the interventricular septum, express barely detectable levels of Cx43 but an abundance of Cx40 and Cx45 (Figure 17). The prevalence of Cx43 in the working myocardium but near absence in the proximal VCS suggests that this pattern could be important for electrical insulation of the conduction tissue (Gourdie et al. 1993).

II. Results and Discussion

In the absence of detectable changes in tissue morphology and size, we tested whether changes in cell behavior could account for the observed conduction defects. Cellular excitability and intercellular coupling were examined and compared in Irx3 null and control mice. Cells isolated from the proximal VCS of neonatal Irx3 null and wildtype littermate hearts were examined by live calcium imaging (Figure18). In wildtype cultures, the majority of Irx3::EGFP^{+} cells were observed to drive depolarization of neighboring non-GFP cells. In the absence of Irx3, Irx3::EGFP^{+} and non-GFP cells depolarized neighboring cells equally well.

Quantitation of genes expression changes in FACS (based on Irx3::EGFP expression) sorted Irx3 null and wildtype cell populations at postnatal day 3 reveal altered expression of genes that regulate automaticity and the depolarizing phase of the action potential (Figure 19). Transcript levels for Hcn4 (hyperpolarization-gated, cyclic nucleotide-gated family potassium channel 4), which is normally highly expressed in the VCS, were significantly decreased in cells lacing Irx3. Furthermore, adenoviral overexpression of Irx3 in neonatal ventricular myocytes resulted in increased Hcn4 mRNA expression in comparison to the Ad-LacZ control and uninfected cells (Figure 19 c,d). These data suggest that Irx3 is required for Hcn4 expression.

Abnormal expression of genes encoding channel subunits of the depolarizing sodium current (I_{Na}) was also observed. In the absence of Irx3, mRNA of Scn5a (sodium channel, voltage-gated, type V, alpha subunit) was decreased in cells lacking Irx3 (Figure 19b). The pore-forming channel subunit Scn5a is not only highly enriched in the VCS, but is also an important determinant for the rate of membrane depolarization (Remme et

al. 2009). Moreover, the auxiliary beta subunit, Scn1b (sodium channel, voltage-gated, type I, beta) was significantly increased in cells lacking Irx3. Interestingly, Scn1b is also progressively enriched in the VCS during development and losses of function mutations have been shown to lead to reduced I_{Na} and inherited conduction system disease (Watanabe et al., 2008, JCI). Importantly, Scn1b can modulate sodium current density by affecting Scn5a gating and channel expression in cell systems (An et al. 1998; Dhar Malhotra et al. 2001; Isom 2001; Dominguez et al. 2005). Abnormal expression of these ion channel genes could account for the observed decrease in cellular excitability. Further experiments are aimed at precisely measuring changes in membrane excitability using single cell recording approaches, and determining whether these genes are direct transcriptional targets of Irx3.

The specific expression levels and pattern of Cxs that compose VCS gap junctions is thought to ensure efficient coupling within this specialized tissue compartment, while functionally insulating it from the working myocardium (Gourdie et al. 1993). We used laser capture microdissection and fluorescence from Cx40EGFP mice to isolate Purkinje fibers along the ventricular free walls (Figure 20 a-g). We found that Cx40 mRNA (*Gja5*) was significantly lower in the Purkinje fibers of $Irx3^{tauLacZ/tauLacZ}$;$Cx40^{EGFP/+}$ mice compared to that of their $Cx40^{EGFP/+}$ littermates, revealing less than expected mRNA expression from the remaining Cx40 allele in the absence of Irx3 (Figure 20h). Furthermore, immunofluorescence and confocal microscopy showed that Cx40 protein, which is normally expressed throughout the VCS in neonatal hearts, was reduced in mice lacking Irx3 (Figure 20i).

However, the observed decrease in Cx40 cannot fully account for the ventricular activation phenotype because hearts from *Cx40*$^{EGFP/+}$ mice show normal heart activation (Kirchhoff et al. 1998; Simon et al. 1998; Bevilacqua et al. 2000). In addition to reduced Cx40, we detected ectopic Cx43 expression in the proximal bundle branches, marked by Irx3::EGFP, where only nominal expression of Cx43 normally occurs (Figure 21a,b). High-resolutionn imaging of immunofluorescently labelled tissue at 100x magnification revealed ectopic Cx43 expression at cell borders between Irx3::EGFP^{+} VCS myocytes, and between non-GFP working myocytes and VCS myocytes (Figure 21c). Cell pairs from reaggregated neonatal myocytes isolated from the proximal VCS were analyzed for clear Cx43 plaque expression at cell-cell borders marked by N-cadherin. In the absence of Irx3, a higher number of cell borders between VCS cells (Irx3::EGFP^{+}) and non-GFP working myocytes contained Cx43^{+} plaques compared to wildtype (Figure 22).

To better understand how the observed changes in Cx expression could underlie conduction slowing, we employed a dye-coupling assay (Lisewski et al. 2008) in which the spread of Alexa594 from microinjected cells of the proximal right bundle branches was measured to examine intercellular communication. Dye spread was predominantly restricted within Irx3::EGFP^{+} VCS cells in wildtype hearts, whereas *Irx3*$^{tauLacZ/tauLacZ}$ hearts displayed significantly higher depth of dye spread from bundle branch cells to the non-GFP working myocardium (Figure 21d,e). These data complement our immunofluorescence results, which demonstrates altered expression levels of Cx40 and Cx43, and provides evidence for abnormal communication between VCS cells and the working myocardium which predominately express Cx43.

Hemichannels with heterogeneous Cx isoform composition due the observed changes in Cx40 and Cx43 expression could account for the conduction defect in mice lacking Irx3. Formation of functional gap junctions containing heterogeneous Cx40 and Cx43 isoforms, albeit with altered conductances in comparison to homomeric/homotypic junctions, has been successfully demonstrated in cell systems (Cottrell and Burt 2001; Valiunas et al. 2001; Cottrell and Burt 2005). In our case, abnormal communications between cells of the proximal VCS to those of the working myocardium, via various possible Cx43-containing gap junctions, is expected to lead to impulse dispersion away from the conduction axis, and formation of an unsafe conduction pathway between the VCS (small source of excitation) and the much larger working myocardium (large sink).

To examine whether ectopic Cx43 could account some or all of the observed ventricular activation phenotype, a genetic rescue experiment was devised for future analysis. Heart-specific knockout of Cx43 was generated by crossing of *Mef2CAHF::Cre;Irx3*$^{tauLacZ/+}$ mice with *Gja1*$^{flox/flox}$*; Irx3*$^{tauLacZ/+}$ mice. Surface ECG analysis will be carried out to determine whether mice homozygous for the Irx3 null allele and heterozygous for Gja1 could result in complete or partial rescue of the QRS prolongation ECG phenotype expected for littermates homozygous for *Irx*3.

IV Figures

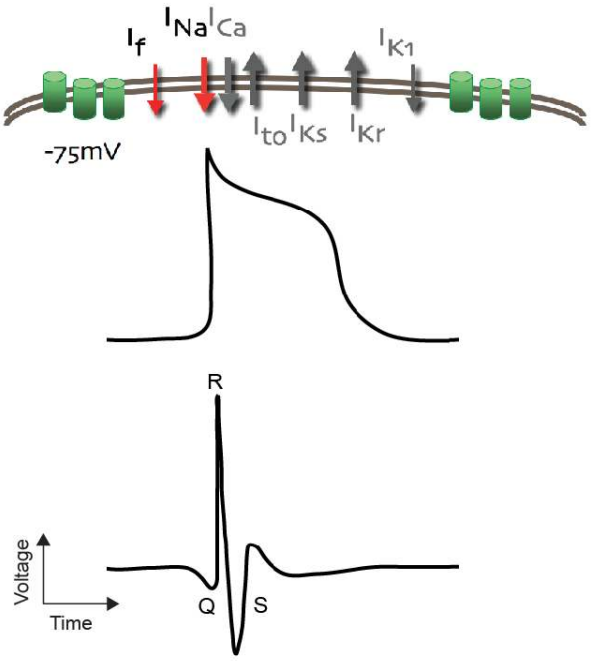

Figure 15. A schematic of the cardiac action potential time course, the underlying ionic currents across the cell membrane, and the matching ECG sequence.

Figure 15. A schematic of the cardiac action potential time course, the underlying ionic currents across the cell membrane, and the matching ECG sequence.

The efficiency of action potential firing is largely dependent on the inward sodium current (I_{Na}) which dictates the rate of membrane depolarization, and the ability of the cell to spontaneously reach the firing threshold. This in turn, is determined by the pacemaking current (I_f) encoded by the hyperpolarization-gated, cyclic nucleotide-gated family of channels.

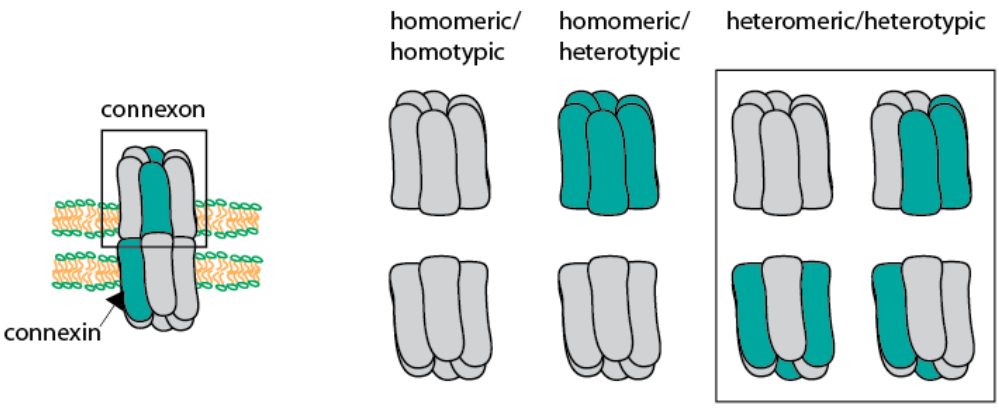

Figure 16. Gap junction composition. (Adapted from Cottrell and Burt, 2005)

Figure 16. Gap junction composition.

The docking of 2 connexons from adjacent cells forms a gap junction channel. Each connexon is a hexamer containing 6 connexin isoforms. Depending on the isoform composition of each connexon, homomeric and heteromeric hemichannels can be formed. Moreover, depending on whether docking hemichannels are of the same type of connexon, homotypic and heterotypic gap junctions can be formed.

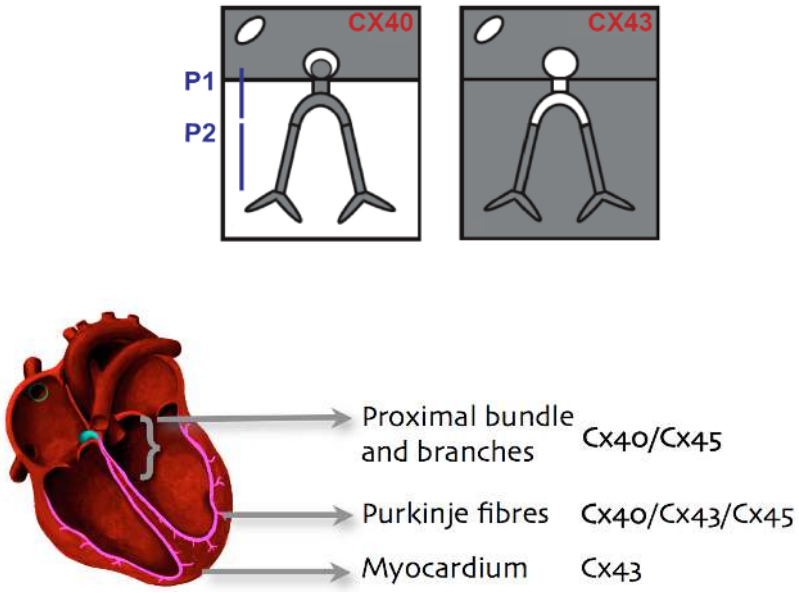

Figure 17. Cx40 and Cx43 expression patterns in the heart and ventricular conduction system.

Figure 17. Cx40 and Cx43 expression patterns in the heart and ventricular conduction system.

Cx40 is expressed in the atria and the VCS, but is absent in the SA node and AV node. Cx43 is expressed throughout the working myocardium of the ventricles and atria, but is absent from the SA node and the proximal VCS. The distribution of Cx40, Cx43, and Cx45 throughout the VCS is also show. P1, proximal portion of the VCS; P2, distal portion of the VCS. (Cole et al. 1988; Saez et al. 2003)

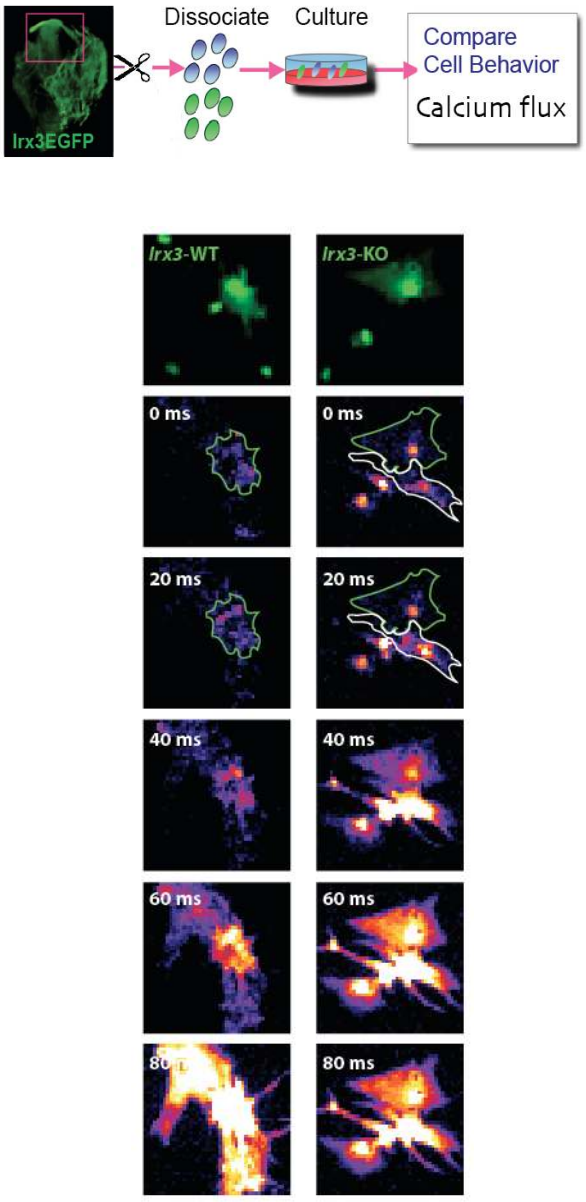

Figure 18. Reduced excitability in Irx3::EGFP^{+} VCS cells lacking Irx3.

Figure 18. Reduced excitability in Irx3::EGFP^{+} VCS cells lacking Irx3.

In Irx3WT cultures, the majority of Irx3EGFP^{+} cells isolated from the proximal VCS drive depolarization of neighbouring non-GFP cells. In the absence of Irx3, Irx3EGFP^{+} and non-GFP cells can depolarize similarly sized clusters equally well. Representative calcium flux images for wildtype and Irx3 null cells are shown.

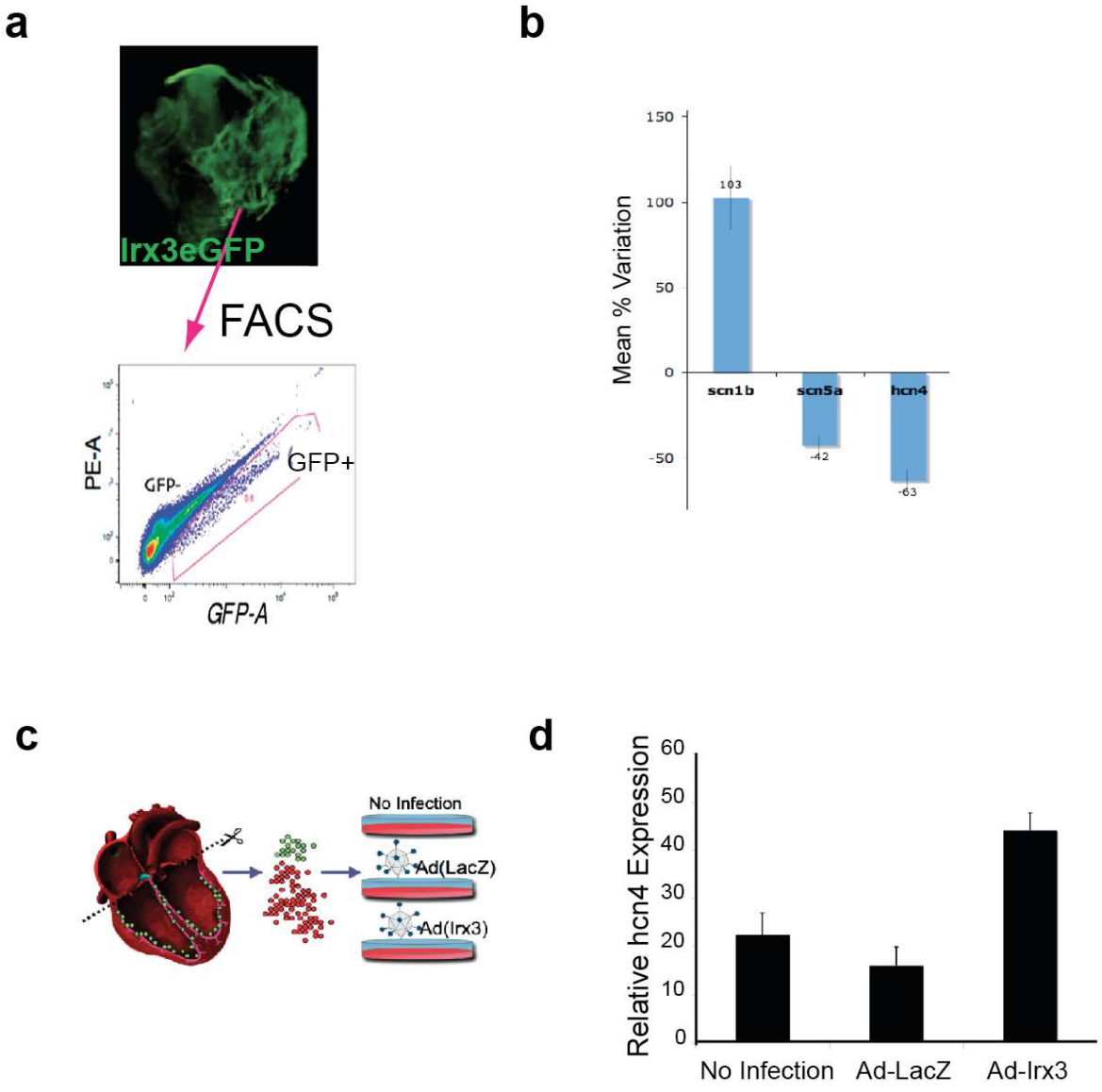

Figure 19. Loss of Irx3 leads to altered expression of ion channel-encoding genes.

Figure 19. Loss of Irx3 leads to altered expression of ion channel-encoding genes.

a, The Irx3::EGFP reporter was used to obtain GFP+ and non-GFP cell populations in wildtype and Irx3 null mice. **b**, Quantitation of gene expression by qPCR shows significant changes in Scn5a, Scn1b, and Hcn4 in cells lacking Irx3. Expression levels were normalized to GAPDH. *$p < 0.05$ versus WT. **c**, Neonatal ventricular myocytes were infected with adenoviruses overexpressing Irx3 and LacZ. **d**, Irx3 overexpression led to significantly higher Hcn4 mRNA at 48 hours post infection in comparison to Ad-LacZ control and uninfected cells. Expression levels were normalized to GAPDH. *$p < 0.05$ versus non-infected.

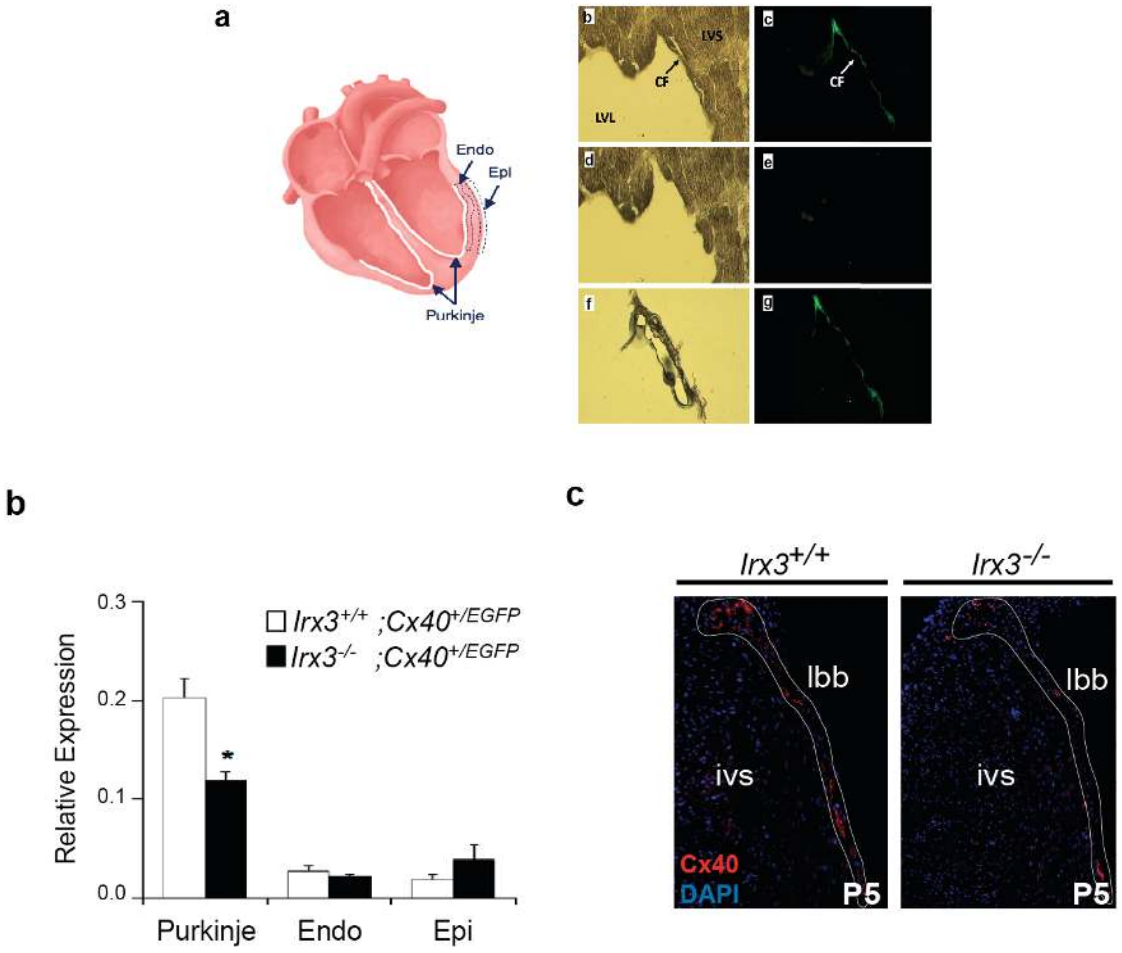

Figure 20. Loss of Irx3 leads to decreased Cx40 expression.

Figure 20. Loss of Irx3 leads to decreased Cx40 expression.

a, Diagram depiction of where cells were isolated for LCM. **b-c**, Prior to laser capture. **d-e,** Following laser capture of conduction fiber. **f-g**, Isolated conduction fiber located on the LCM capsule. **h,** qPCR analysis of LCM captured adult VCS cells reveal decreased *Gja5* mRNA in $Irx3^{tauLacZ/tauLacZ};Cx40^{EGFP/+}$ hearts (normalized by GAPDH); *, $p < 0.05$ vs. $Irx3^{+/+};Cx40^{EGFP/+}$. i**,** Immunofluorescence detection shows decreased Cx40 protein expression in the VCS of Irx3 null mice at P5. LVL, left ventricular lumen; LVS, left ventricular septum; CF, conduction fiber.

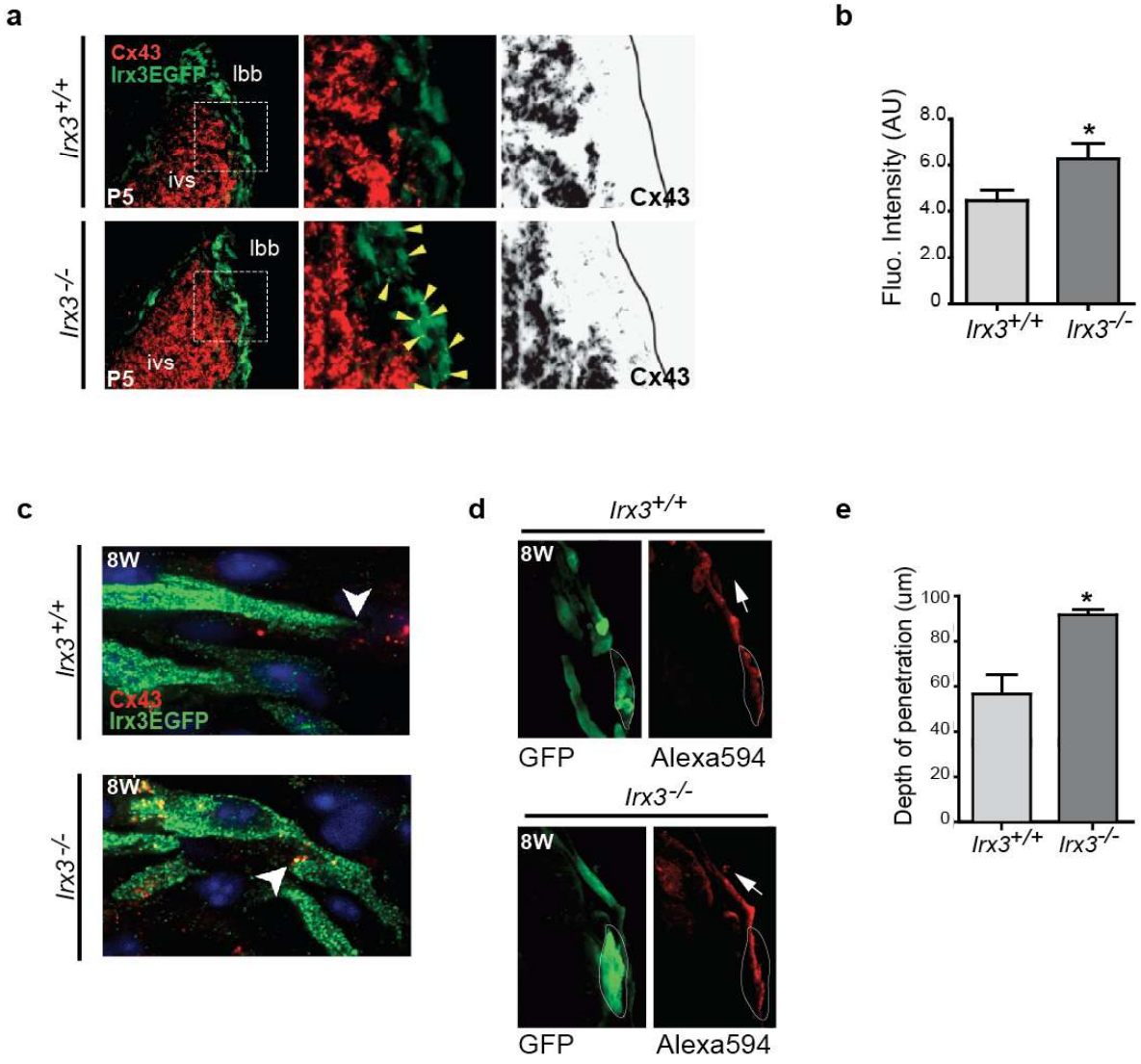

Figure 21. Loss of Irx3 leads to ectopic Cx43 expression.

Figure 21. Loss of Irx3 leads to ectopic Cx43 expression.

a, Ectopic $Cx43^{+}$ plaques are found in Irx3::$EGFP^{+}$ proximal bundle branch cells of Irx3 null mice. **b.** Plaque intensity was quantified using the ImageJ software. *, $p< 0.05$ versus wildtype. **c,** Confocal imaging at 100x magnification shows ectopic $Cx43^{+}$ plaques at conduction-working myocyte, and conduction-conduction myocyte borders in the absence of Irx3. **d-e,** Fluorescent dye spread in microinjected proximal right bundle branch cells (marked by Irx3::$EGFP^{+}$) is mostly within Irx3::$EGFP^{+}$ cells in wildtype hearts, whereas significantly more dye spread into the working myocardium in Irx3 null hearts. *, $p< 0.05$ versus wildtype.

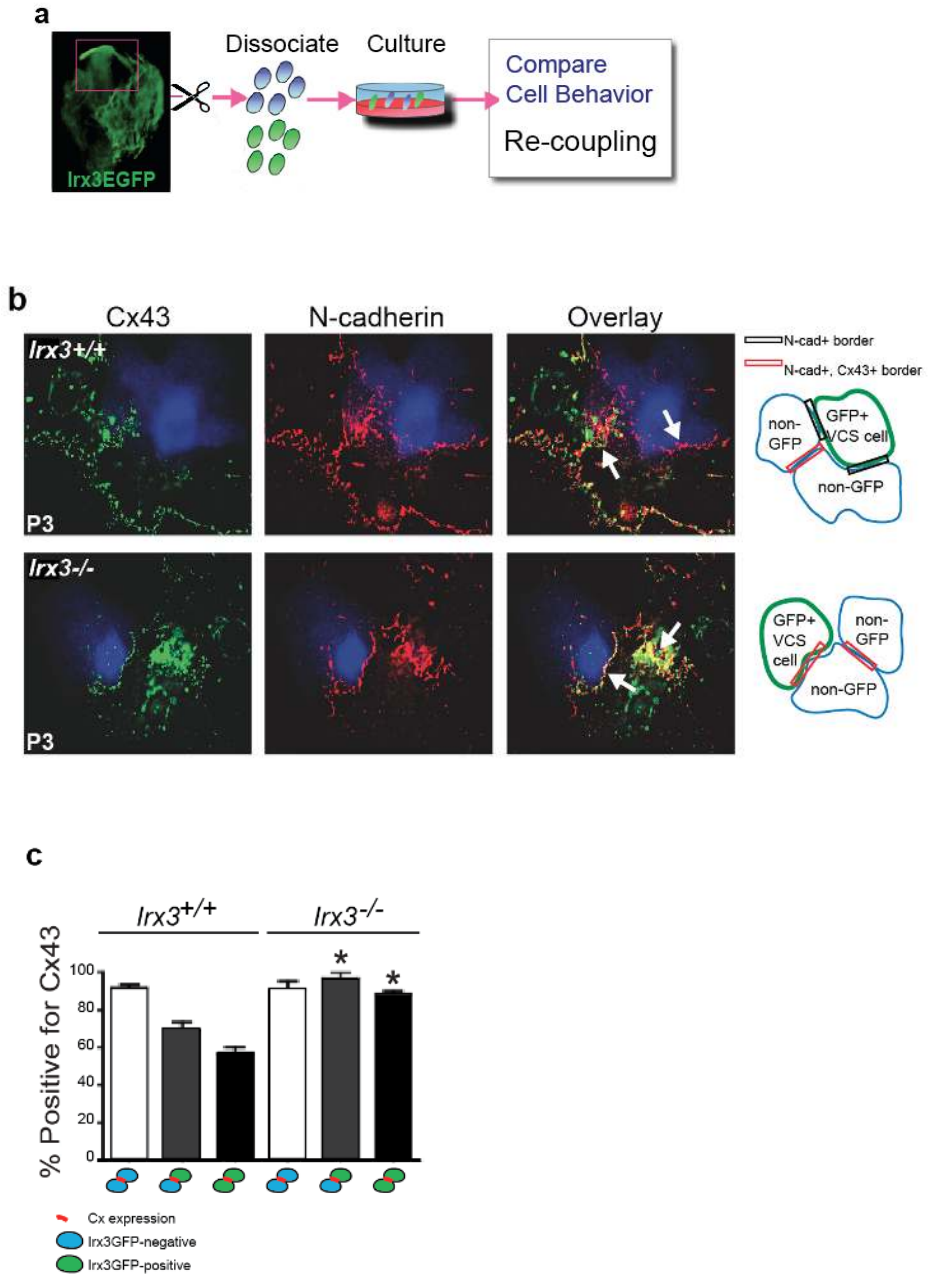

Figure 22. In the absence of Irx3, cultured VCS cells re-couple to working myocytes via Cx43^{+} cell borders.

Figure 22. In the absence of Irx3, cultured VCS cells re-couple to working myocytes via Cx43^{+} cell borders.

a, Diagram depiction of the location from which proximal VCS were isolated at P3. Cells from either wildtype or Irx3 null mice, each expressing the Irx3::EGFP reporter, were isolated and cultured in DMEM:F12 for 8 hours before immunocytochemistry. **b**, Cell pairs were analyzed for clear Cx43 plaque expression at cell-cell borders. In the absence of Irx3, a higher number of re-aggregated Irx3::EGFP^{+} cells (blue) from the proximal VCS re-coupled to Irx3::EGFP^{-} working myocytes via Cx43 (green) at cell borders (marked by N-cadherin, red). c, Quantitation of clear Cx43 plaque expression at cell-cell borders show that a significantly higher number of VCS (Irx3::EGFP^{+}) cells expressed Cx43 at cell borders in the absence of Irx3. n = 80, *, $p < 0.05$ versus wildtype.

CHAPTER 4

Regulation of Cx43 and Cx40 Gene Expression by Irx3

I. Background

Studies to date support a causal relationship between locally acting transcription factors and early patterning of the conduction system, as well as the establishment of regionalized expression of genes involved in cardiac electrophysiology (Boukens et al. 2009). A reduction or absence of these transcription factors causes various heart defects that include improper formation and function of parts of the conduction system. For example, the transcription factors Tbx5 and Nkx2-5, which are expressed in elevated levels in the proximal VCS primordium in comparison to the ventricular working myocardium, are required for activation of fast-conduction system markers (Thomas et al. 2001; Moskowitz et al. 2007). Furthermore, the transcriptional repressor Tbx3 was demonstrated to participate in early specification of the His bundles by repressing markers of working myocardium (Hoogaars et al. 2004; Bakker et al. 2008).

A late wave of VCS maturation, which begins right after birth and involves bundle branch remodeling, has been shown to depend on Nkx2-5 expression in conduction myocytes (Meysen et al. 2007). An additional example of a transcriptional repressor that functions to regulate heart conduction is *Irx5*, which was shown to repress Kv4.2 transcription to establish an epi-endocardial gradient of this potassium channel subunit important for ventricular repolarization. Insights into the regulation of Cx40 and Cx43 expression by Irx3 are presented in this final chapter.

II. Results and Discussion

To gain mechanistic insight into Irx3 function as a transcriptional regulator, we examined Cx40 (*Gja5*) and Cx43 (*Gja1*) expression in isolated neonatal ventricular myocytes (NVMs) infected with adenovirus encoding GFP, Irx3, dominant Irx3 activator (*VP16-Irx3*), or dominant Irx3 repressor (*EnR-Irx3*) (Figure 23 a). Infected NVMs overexpressed comparable levels of Irx3 mRNA (figure 23b) and protein (Figure 23c). Overexpression of *Irx3* in HeLa cells led to a significant decrease in endogenous Cx43 expression in a dose dependent manner (Figure 24a). Overexpression of Irx3 in NVMs, but not the Ad-LacZ negative control, resulted in decreased Cx43 protein levels. Changes in Cx43 protein corresponded to decreased transcript levels, suggesting that Irx3 represses transcription of Cx43 (Figure 24b-d).

Consistent with the observed Cx40 decrease, *Gja5* expression in NVMs was increased by Irx3 overexpression (Figure 25a,b). Interestingly, *EnR-Irx3* overexpression promoted *Gja5* expression, whereas *VP16-Irx3* inhibited *Gja5* expression. These results suggest that Irx3 likely regulates *Gja5* indirectly, and activates *Gja5* expression by suppressing the transcription of a *Gja5* repressor. In contrast, our NVM infection results indicate that Irx3 directly represses *Gja1* transcription.

In agreement with a repressive role of Irx3 on Cx43 expression *in vivo*, *Gja1* mRNA and Cx43 protein were reduced in cells overexpressing Irx3 (Figure 25a,b). Furthermore, *Gja1* mRNA decreased drastically in the presence of *EnR-Irx3* but increased slightly in response to *VP16-Irx3*. The effects of dominant repressor and activator forms of Irx3 on the connexin promoters is summarized in Figure 25c. Given that *Iroquois* proteins commonly act as transcriptional repressors, our data support antithetical regulation of

Cx40 and Cx43 expression by Irx3 through direct as well as indirect mechanisms.

Promoter analysis of connexins that are expressed in the VCS (Cx40, Cx43, Cx45, Cx30.2) revealed that only the *Gja1* promoter contains an evolutionarily conserved element harboring a putative Irx3 binding site (Bilioni et al. 2005; Berger et al. 2008; Noyes et al. 2008), which overlaps with an Nkx2-5 binding motif (Irx/NKE) immediately upstream of a conserved T-box binding element (Figure 26a). Co-immunoprecipitation show that Irx3 can form a protein complex with Nkx2-5 and Tbx5 (Figure 26b). To determine if Irx3 binds the *Gja1* promoter *in vivo*, we performed chromatin immunoprecipitation with ventricles isolated from an $Irx3^{3myc\text{-}6his}$ knock-in mouse line, which expresses a C-terminally tagged Irx3 protein under all potential endogenous gene expression control elements (Figure 27).

Enrichment for Irx3-3myc-6his was detected at the *Gja1* promoter region containing the Irx/NKE element and the core *Gja1* promoter, but not at an intergenic region of *Gja1* or at the *Nppa* promoter (Figure 28a). We found that Irx3 antagonizes Tbx5- or Nkx2-5-dependent activation of a *Gja1-luciferase* reporter in COS7 cells transfected with Irx3, Nkx2-5, and Tbx5 in combination (Figure 28b). This repression is dosage sensitive and specific to the *Gja1* promoter but not to the *Nppa* promoter (Data not shown). Potential interaction of *in vitro* synthesized Nkx2-5 and Irx3 with the conserved *Irx/NkE* element was tested by electromobility shift assays (EMSAs, data not shown). Nkx2-5 or Irx3 was bound to the conserved element and the respective positive controls. However, when the Irx3 binding site was mutated, binding was abolished. Further experiments are aimed at determining whether a mutated binding site could prevent the *Irx3*-dependent repression of *Gja1-luciferase* expression.

These results suggest that in cells that express all 3 transcription factors at high levels, such those from the proximal VCS, Irx3 can repress Nkx2-5- and Tbx5-mediated activation of *Gja1* transcription (Figure 28c). Whether direct binding of Irx3 to the *Gja1* promoter could lead to transcriptional repression via inhibitory protein-protein interactions with Nkx2-5 or Tbx5, and/or via recruitment of co-repressors through a mechanism similar to that of Irx5(Costantini et al. 2005), remains to be tested.

We establish here that Irx3 is a novel transcriptional regulator of rapid electrical conduction that drives ventricular activation, and could be an important candidate gene in congenital or acquired conduction system diseases. Irx3 expression in the heart is highly enriched in the specialized ventricular conduction system cell type, and is required for tight regulation of Cx gap junction gene expression. Regulation of connexin expression by Irx3 is likely to be relevant to other excitable cell types such as specific cells of the central nervous system that also express Irx3. The function of Irx3 exemplifies the importance of precise transcriptional control in establishing efficient impulse conduction.

IV. Figures

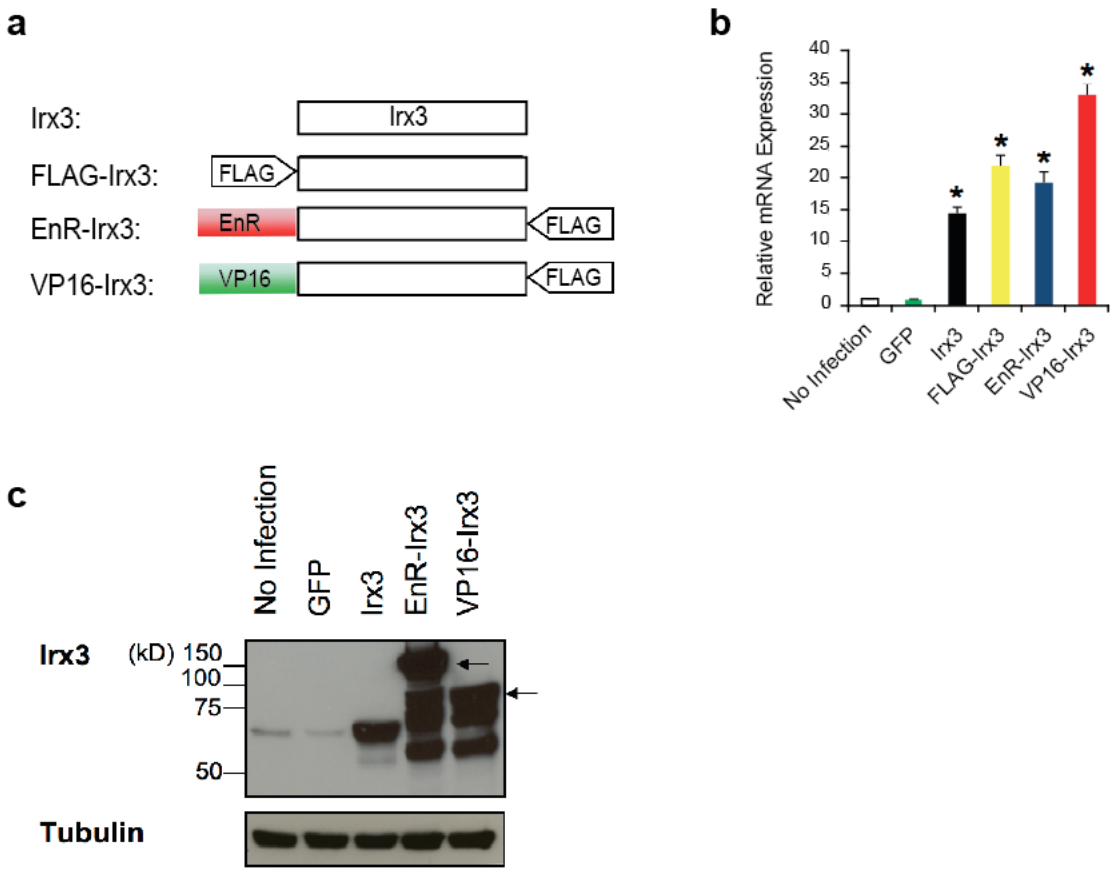

Figure 23. Adenoviral overexpression of *Irx3* constructs.

Figure 23. Adenoviral overexpression of *Irx3* constructs

a, NVMs were infected with the following adenoviral constructs: GFP control (*Ad-GFP*), Irx3 (*Ad-Irx3*, *Ad-FLAG-Irx3*), Irx3 fused to the VP16 activation domain (*Ad-VP16-Irx3*) or the Engrailed suppressor domain (*Ad-EnR-Irx3*). **b**, Irx3 mRNA was expressed at similar levels in NVMs infected with adenoviruses carrying the various overexpression constructs. **c**, Western blot shows successful protein overexpression in infected cells.

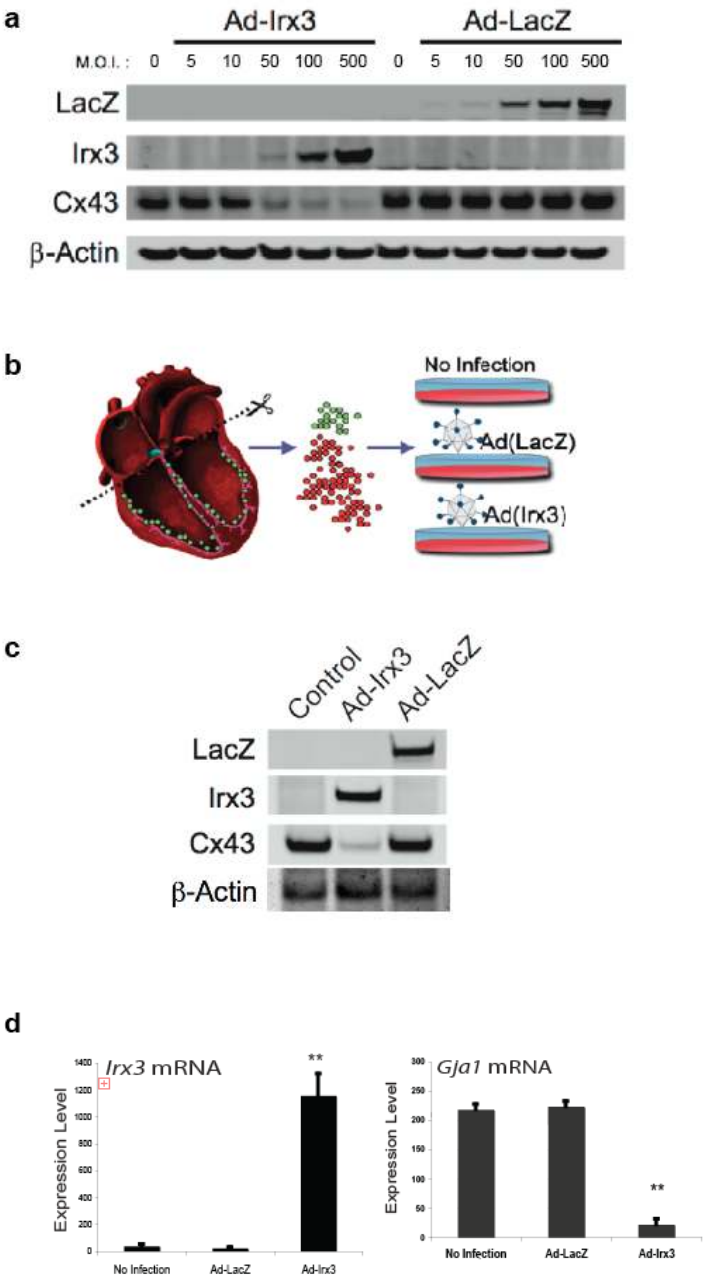

Figure 24. Irx3 overexpression leads to decreased Cx43 in HeLa cells and neonatal ventricular myocytes

Figure 24. Irx3 overexpression leads to decreased Cx43 in HeLa cells and neonatal ventricular myocytes

a, Irx3 overexpression in HeLa cells led to Cx43 repression in a dose dependent manner. **b**, Schematic illustration of adenoviral infection of neonatal ventricular myocytes by viruses carrying wildtype *Irx3* and *LacZ* control. **c**, Adenoviral infection of NVMs at MOI of 5 resulted in marked decrease of Cx43 protein. **d**, qPCR quantitation shows that overexpression of *Irx3* mRNA leads to an increase in *Gja1* at the transcript level.

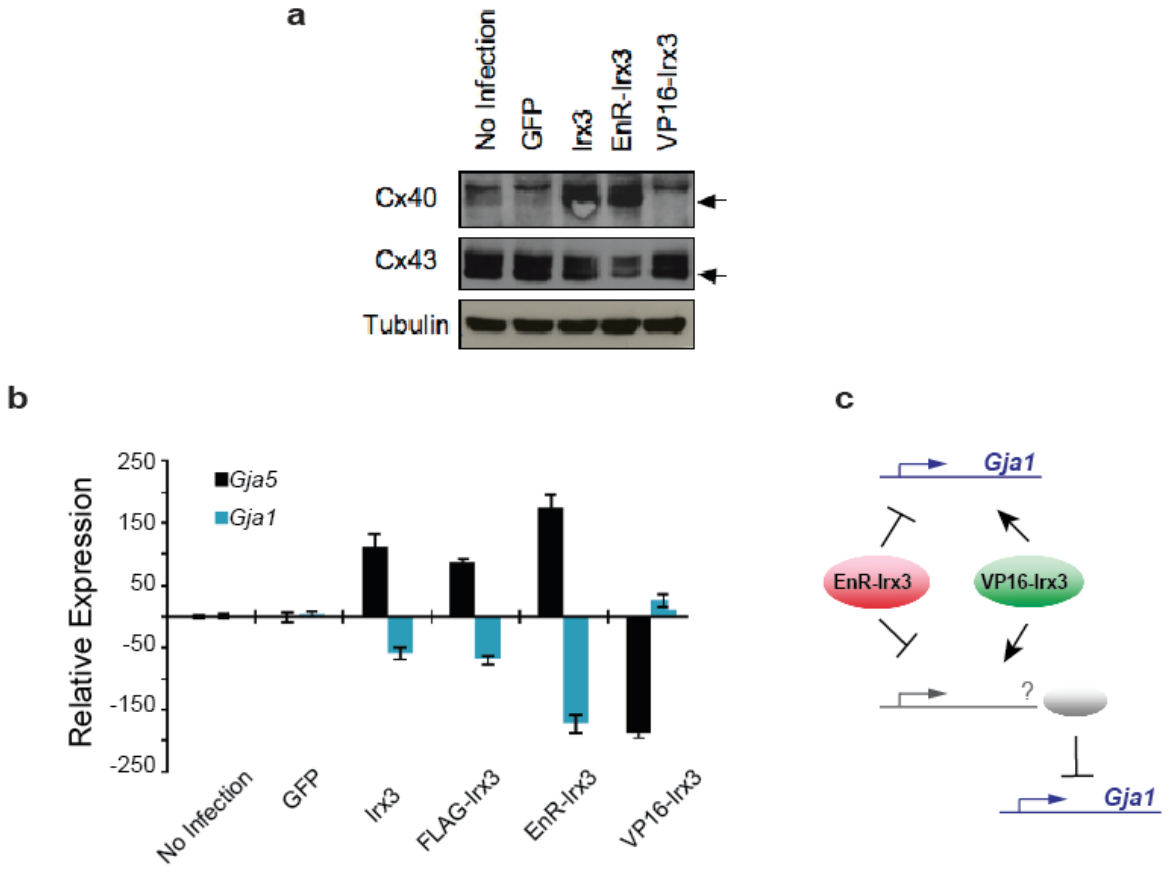

Figure 25. Changes in Cx40 and Cx43 expression in response to adenoviral overexpression of various forms of Irx3

Figure 25. Changes in Cx40 and Cx43 expression in response to adenoviral overexpression of various forms of Irx3.

a, Cx40 protein expression was elevated in Irx3 over-expressing cells compared to controls. Cx40 levels increased in the presence of EnR-Irx3, and decreased upon infection with VP16-Irx3. Cx43 decreased in cells overexpressing Irx3 and dominant negative EnR-Irx3, but increased in response to dominant active VP16-Irx3. **b**, Adenoviral overexpression of Irx3 led to marked increase in *Gja5* mRNA compared to non-infected and GFP-infected cells. However, dominant negative Irx3 (EnR-Irx3) overexpression increased *Gja5* mRNA, while dominant active Irx3 (VP16-Irx3) resulted in decreased *Gja5* expression. Adenoviral overexpression of Irx3, FLAG-Irx3, and EnR-Irx3 leads to marked decrease in *Gja1* expression. Dominant active VP16-Irx3 significantly elevates *Gja1* mRNA. **c**, Schematic depicting regulation of Cx40 and Cx43 transcription by dominant active and dominant negative forms of Irx3.

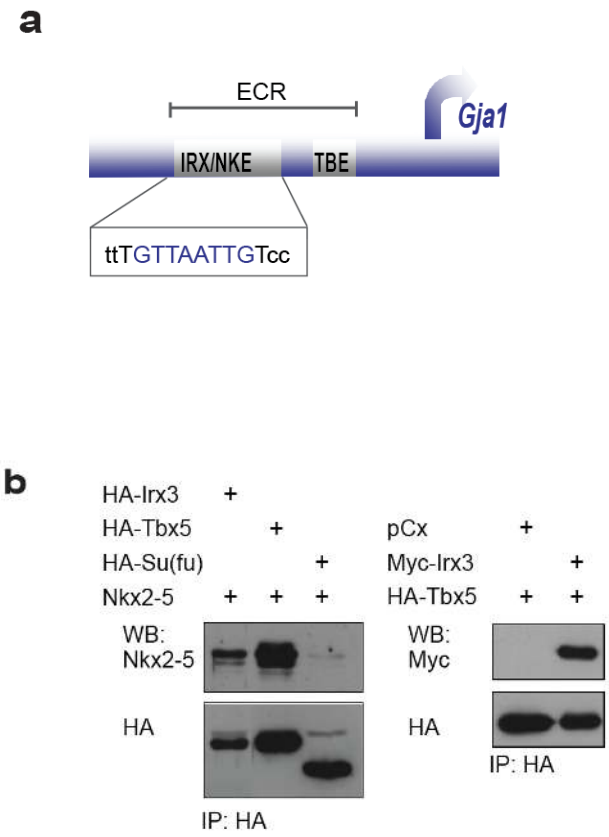

Figure 26. An evolutionarily conserved binding element for Irx3 and Nkx2-5 resides in the *Gja1* promoter.

Figure 26. An evolutionarily conserved binding element for Irx3 and Nkx2-5 resides in the *Gja1* promoter.

a, Genome alignment analysis of the *Gja1* promoter revealed an evolutionarily conserved element containing a putative Irx3 binding site that overlaps with an Nkx2-5 binding motif (Irx/NKE). This is immediately upstream of T-box binding elements (TBE). **b,** Co-immunoprecipitation shows that Irx3 can form a complex with Nkx2-5 and Tbx5.

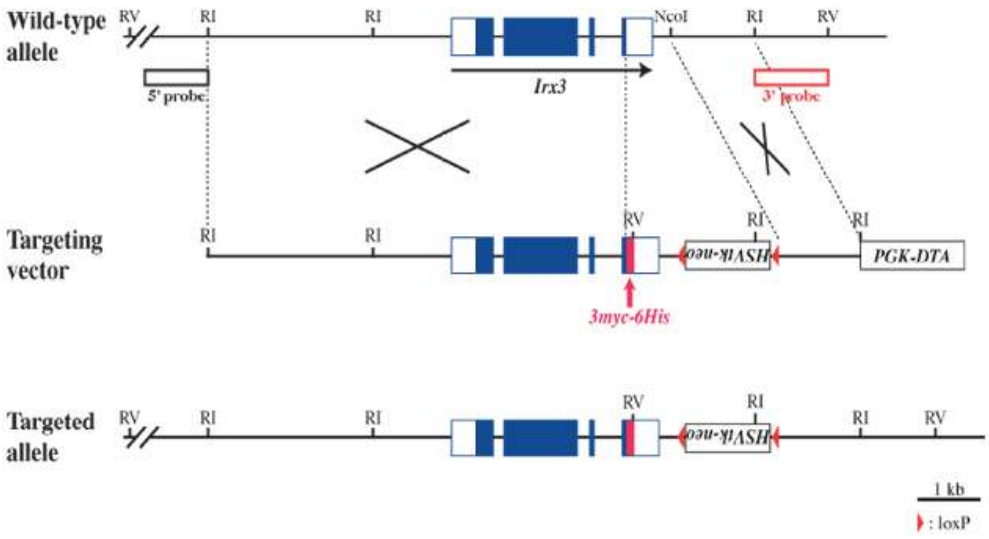

Figure 27. Gene targeting strategy for generating Irx3^{3myc6his} mice.

Figure 27. Gene targeting strategy for generating Irx3^{3myc6his} mice.

Generation of Irx3-3myc-6his mice was achieved by inserting 3 myc-tags and 6 histidines at the C-terminus of Irx3. Irx3-3myc-6his protein was detected in whole embryo lysates and the VCS using antibodies against Irx3 and myc-tag (data not shown).

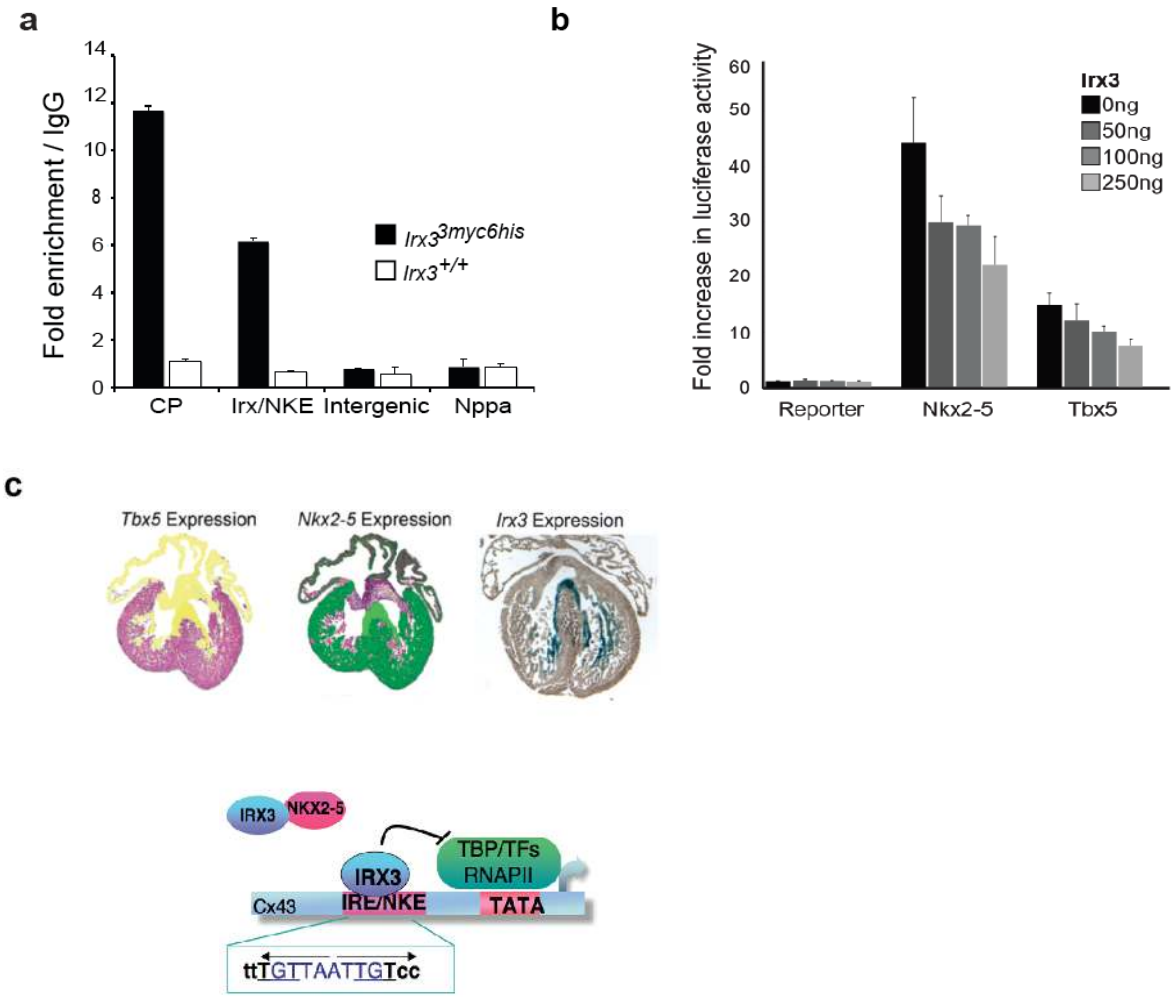

Figure 28. Cx43 is a direct transcriptional target of Irx3.

The top panel of part **c** was adapted from Moskowitz et al., 2007.

Figure 28. Cx43 is a direct transcriptional target of Irx3.

a, Chromatin immunoprecipitation using ventricles from *Irx3*$^{3myc\text{-}6his}$ mice shows enrichment of Irx3 at the conserved Irx/NKE site and core promoter, but not at an intergenic region or the *Nppa* promoter. **b,** Luciferase assays shows that Irx3 antagonizes activation of a *Gja1-luciferase* construct by transfected Tbx5 or Nkx2-5. **c**, A model for *Gja1* transcriptional repression by Irx3 in the proximal VCS where all three transcription factors are all highly enriched. Sufu, suppressor of fused negative control; ECR, evolutionarily conserved region; CP, core promoter; Irx/NKE, evolutionarily conserved binding site for Irx3 and Nkx2-5.

MATERIALS AND METHODS

Gene targeting and mice.

A loss-of-function mutation in *Irx3* was generated in R1 embryonic stem (ES) cells by replacing part of exon 1 with a *tauLacZ* reporter after the start codon. Generation of $Irx3^{3myc\text{-}6his}$ mice was achieved by inserting three myc-tags (EQKLISEEDL) and six histidines at the C-terminus of Irx3. ES cell lines with the desired mutation were identified by Southern analysis and germline transmission was achieved by standard procedures. PCR genotyping of $Irx3^{tauLacZ}$ was carried out using these primers:

GAGTTGGCCGCCTCTGGGTCCCTATCCAAT,

CCCTCTCTCCCGGGTTTCTCTGGCTCTTAC,

GAATTCGCCAATGACAAGACGCTGGGCGGG.

Genotyping of $Irx3^{3myc6his}$ mice was carried out using these primers:

CAAGAAGGGGTGATGAGAGTCGCTGGGCG, and

GGAGAGGGAACCACGGCGAGAAAGGCCTA. $Irx3^{tauLacZ}$ mice were crossed with $Cx40^{EGFP}$ to generate mice for GFP and LacZ co-localization experiments. *ROSA-YFP;* $Irx3^{tauLacZ/+}$ mice were crossed with either *Mef2CAHF::Cre* or *Wnt1-Cre* mice for lineage analysis. All analyses were done on the *C57BL/6* background. Animals were cared for in accordance with national and institutional requirements.

Expression analysis.

Fluorescence *in situ* hybridization in zebrafish was performed as described (Chi et al. 2008). For mice, β-galactosidase and Masson's trichrome staining of fixed embryos and tissue (4% paraformaldehyde, PFA) was carried out using standard methods. Whole-

mount visualization of the conduction fibers was achieved in post-fixed hearts cleared by 1:2 benzyl alcohol to benzyl benzoate (BABB). Optical projection tomography (OPT) imaging of hearts was performed as described (Sharpe et al. 2002). Briefly, hearts were embedded in 1% low-melting agarose (LMP Agarose, Invitrogen), mounted on stainless-steel stubs, dehydrated in methanol, and cleared using BABB. Samples were mounted on a rotating motor and visualized using a Leica FLIII microscope fitted with GFP2 and rhodamine filter sets. Analysis and visualization of OPT data were performed with Amira software (http://www.amira.com/).

Immunofluorescence.

Tissues samples were fixed in 4% PFA, immersed in a sucrose gradient (30%, 20%, 10% sucrose in PBS), and embedded in OCT compound before freezing in a 2-methylbutane and dry ice bath. Four-chambered view serial sections of 8-μm thick were stained with primary antibodies against Hcn4 (Alome Labs), LacZ (Cappel), Cx40 (Chemicon), GFP (Abcam), Cx43 (Sigma), tropomyosin (Hybridoma Bank), PECAM (Hybridoma Bank), Scn5a (Alome Labs), and N-cadherin (BD Biosciences). Depending on the antibody used, incubations were carried out either at room temperature for 2 hours, or at 4 degrees Celsius overnight. Secondary detection was carried out using Alexa488- , Alexa555- , and Alexa 647-conjugated antibodies (Invitrogen). Nuclei detection and slide mounting were achieved using ProLong ImmunoGold reagent containing DAPI (Invitrogen).

Myocyte isolation.

P1-P3 stage hearts were harvested and digested with 0.25 mg/mL trypsin (Invitrogen) and 50 U/ml type II collagenase (Worthington) in calcium- and bicarbonate-free Hank's buffer with HEPES (HBSS) at 37°C. Non-myocytes were minimized by differential plating for 1 hour as well as by adding 0.1 mM bromodeoxyuridine (BrdU) and 20 μM arabinosylcytosine (Ara-C) in culture medium to inhibit cell proliferation.

Cell assays.

Myocytes from the proximal VCS, at embryonic day 14.5 and postnatal day 3, were dissociated as described above. Cells from either wildtype or Irx3 null mice, each expressing the *Irx3::EGFP* reporter, were isolated and cultured in DMEM:F12 media for 8 hours before calcium flux assays and immunocytochemistry. Cells were fixed for 30 min in 4% PFA before immunofluorescence detection using antibodies against Cx40 and Cx43 as described above. Widefield epifluorescence was performed using a Nikon Eclipse *Ti* microscope with 60x/1.49 Apo TIRF objective and a Coolsnap HQ^2 camera controlled by NIS elements software (Nikon). Cell pairs were analyzed for clear connexin plaque expression at cell borders and quantified. For calcium flux assays, the culture medium was replaced with HBSS containing 2% fetal bovine serum, and GFP^+ cells were identified by widefield epifluorescence. Fluo-4AM (5mM, Invitrogen) was then added to the chamber. Cells were incubated for 15 min before imaging and data acquisition. Images for calcium flux movies were acquired at a rate of 100 fps using a Nikon Eclipse *Ti* microscope with 20x/0.75 Plan Apo objective, and Cascade II 512 camera controlled by NIS elements software. After image acquisition, Hoechst 33258 (Invitrogen) was added to medium to visualize nuclei.

Laser capture microdissection.

Hearts were obtained from adult *Irx3*$^{+/+}$;*Cx40*$^{EGFP/+}$ and *Irx3*$^{tauLacZ/tauLacZ}$;*Cx40*$^{EGFP/+}$ mice. Frozen tissue sections, 10 μm thick, were collected and dehydrated. GFP-positive VCS cells were visualized and captured onto a CapSure Macro LCM cap (Molecular Devices, Sunnyvale, CA) with a PixCell II System equipped with epifluorescence optics (Arcturus, Mountain View, CA), a spot size of 7.5 μm, power of 60–80 mV, and pulse duration of 700 μs . Subendocardial and subepicardial cells were also captured on separate caps. RNA was isolated using the Arcturus Pico Pure RNA isolation kit.

Echocardiography.

Transthoracic echocardiography was used for non-invasive serial assessment of cardiac function in mice with a Vevo 770 ultrasound machine (VisualSonics) as described(Zhou et al. 2004; Costantini et al. 2005).

Surface ECG.

Surface ECG (lead I and II) was obtained at P12 and at 8–10 weeks. Three needle electrodes were placed subcutaneously in standard limb lead configurations in adult mice that were anesthetized with 1.75% isoflurane at a core temperature of 36.8 ± 0.3°C. Twenty seconds of continuous signals were sampled at 10 KHz in each lead configuration with a PowerLab4/30 interface (AD Instruments). Data was analyzed offline using electronic calipers on averaged beats (Chart5Pro v 5.4.2, AD Instruments).

The QRS interval was measured from the onset of the Q-wave to the isoelectric point preceding the first rapid repolarization wave. For telemetry ECG, telemetry devices (Data Sciences International; St. Paul, MN) were implanted dorsally with electrodes in lead II configuration. Mice were allowed to recover for 60 h post-surgery before ECG data were collected and analyzed.

Intracardiac ECG.

Intracardiac ECG was measured in anesthetized mice (1.5% isoflurane) while body temperature was maintained around 36.8 ± 0.3°C, using a 2-French octapolar electrode catheter (CIBer mouse EP catheter; NuMed, Hopkinton, NY, USA). Correct catheter placement was confirmed upon visualization of 6 bipolar leads from the catheter, where the most distal lead (1–2) electrogram in the ventricle showed a large ventricular signal with minimal atrial signal, while the most proximal lead (7–8) showed larger atrial than ventricular signals. The His-bundle electrogram was confirmed in the middle leads (4–5 or 5–6), or by visualization of a small deflection (< 1 mV) in between atrial and ventricular signals. All ECG signals were recorded and amplified at 5 kHz and filtered between 0.3 Hz and 300 Hz by a Gould ACQ-7700 amplifier and PONEMAH software.

Optical mapping and analysis.

Activation mapping in zebrafish was performed as described(Chi et al. 2008). Beating hearts from adult 8-10-week-old control and *Irx3*-deficient were isolated and placed into Krebs solution containing (in mmol/L) 118 NaCl, 4.2 KCl, 1.2 KH_2PO_4, 1.5 $CaCl_2$, 1.2 $MgSO_4$, 11 D-glucose, 2 sodium pyruvate, and 25 $NaHCO_3$ bubbled with carbogen (95%

CO_2/5% O_2). Cannulated hearts were perfused with 37°C Krebs solution (pH 7.4) at a constant flow rate of 3.5 ml/min for a 15-minute equilibration period, followed by 10-minute perfusion of voltage-sensitive dye, di-4-ANEPPS. Hearts were excited using an EXFO X-Cite exact source filtered at 543 ± 11 nm, and high-resolution optical images were taken using an upright Olympus MVX-10 microscope equipped with a Photometric Cascade 128+ CCD camera interfaced with ImagePro Plus 5.1 software. Resolution of image sequences captured was 16-bit, 63 x 64 pixel at 923Hz. All mapping studies were performed in the absence of any motion reduction techniques. ECG was also recorded simultaneously. For analyzing optical imaging, a visual basic for applications (VBA) macros for ImagePro Plus 5.1 was used to subtract values of each pixel from the time average for each pixel to get the action potential. After passing the AP through a 3 x 3 pixel spatial averaging kernel, activation time was defined as the time of 50% depolarization during the rising phase of the action potential. Isochronal maps that display the position of the wavefront at constant time intervals (0.5 ms) were constructed from the activation times by the Scroll software. Local velocity vectors were calculated by fitting the depolarization time, measured at each pixel, to a 3x3 pixel plane with least squares and finding their gradients. Conduction velocities were estimated by averaging the absolute values of these gradients.

VCS fiber conduction velocity.

While the hearts was perfused with a modified Krebs-Henseleit solution containing 0.3 mM Ca^{2+} at room temperature, action potentials (AP) were gathered using two fine-tip glass electrodes (A-M Systems model 3100) on the Purkinje fibers identified by *Cx40*

promoter-driven EGFP. Conduction velocity was calculated by the time interval between peaks of two APs divided by the distance between the electrodes.

Connexin imaging and quantitation.

For quantification of Cx40 and Cx43 expression in the VCS, the Scan Large Image function of NIS Elements was employed to stitch high-resolution (60x/1.49 Apo TIRF objective) widefield epifluorescence images encompassing the entire septum. With the ImageJ software, GFP images were converted to binary masks. Within this mask image, GFP^+ regions had a value = 1, and all remaining pixels had a value = 0. Masks were image-multiplied by corresponding Cx40 or Cx43 images to exclude all signals except that from GFP^+ cells, and fluorescence intensity was subsequently measured. To account for slide-to-slide variance, two random 400 x 400 pixel regions of interest were measured in GFP^- regions of the septum. Similarly, background was determined for each image with a 400 x 400 pixel tissue-free region of interest and subtracted from all values. Fluorescence intensity in the proximal VCS was then normalized to that of the septal working myocardium and graphs plotted using Prism 5 software (Graphpad).

Dye injection.

Cardiac slices were prepared from freshly isolated hearts as described (Lisewski et al. 2008). Live 250-μm thick slices were obtained in central 4-chambered view to expose proximal right bundle branches along the septum. Briefly, ventricles were longitudinally cut with the apex removed before embedding in 2.5% low-melt agarose. Samples were glued to the stage of a vibrating blade microtome (Leica) and immersed in Hank's

balanced salt solution (Invitrogen). Sections were transferred to a glass bottom dish, and single bundle branch cells, which are elongated in shape and express the *Irx3::EGFP* reporter, were identified by wide-field epifluorescence microscopy. For microinjection, glass micropipettes (Femtotips II; Eppendorf) were loaded with 5 mM AexaFluor594 hydrazide sodium salt (Invitrogen) in 200 mM KCl. Individual GFP^+ cells were microinjected at 50 hPa pressure for 0.2 sec with a FemtoJet apparatus (Eppendorf) and micromanipulator. Four minutes post injection, sections were fixed in 4% PFA overnight at 4ºC. Tissues were processed for GFP reporter detection with the chicken anti-GFP antibody (Abcam) and AlexaFluor647 goat anti-chicken secondary antibody (Invitrogen). Z-stacks of mounted sections were acquired by spinning disc confocal microscopy with a Nikon T*i* microscope with a 20X/0.75 Plan Apo objective, Yokogowa CSU-X1 spinning disk confocal unit with 561- and 647-nm DPSS laser sources and a Coolsnap HQ^2 camera controlled by NIS Elements software. Nikon Eclipse *Ti* microscope had a 20x/075 plan Apo objective and Coolsnap HQ^2 camera controlled by NIS elements software. Maximum intensity projections of 25-μm Z-stacks (0.5-μm intervals) were generated, and dye penetration measured using ImageJ software (NIH).

Adenoviral Construct Generation.

Adenoviral Irx3 constructs were generated using Adeno-X ViraTrak Expression System 2 (Clontech). The mouse cDNA encoding the entire Irx3 was fused with FLAG-tag, the VP16 activation domain, and the Engrailed suppressor (EnR) domain at the N-terminus of Irx3. These were then sub-cloned into the Creator Donor vector pDNR-CMV. Sequence between two loxP sites of pDNR-CMV vector was transferred into the single

loxP site in the adenoviral genome of the Adeno-X ViraTrak Acceptor vector by Cre recombinase. After selecting recombinants with chloramphenicol, the recombinant adenoviral genome was released by enzyme digestion with PacI to produce infectious recombinant adenoviruses which were transfected into low-passage HEK-293 cells. Two days later, transfection efficiency was visually confirmed under fluorescent microscope. 7–10 days later, recombinant adenoviruses were harvested and stored in -80°C after titers were determined.

Adenoviral infection.

After culturing in 10% serum medium for 24 hours, NVMs were infected for 3–4 hours with adenovirus at a multiplicity of infection (MOI) of 5 and cultured in fresh serum medium. At day 4, cells were harvested for quantitative PCR or protein experiments.

Luciferase reporter gene assays.

Transfections and Luciferase assays were performed as described(Costantini et al. 2005). Briefly, COS7 cells were grown in Dulbecco's Modified Eagle's Medium supplemented with 10% fetal bovine serum to 80% confluency before transfection. 500ng of each plasmid DNA was transfected using Fugene HD (Roche Applied Science). Luciferase activity was measured at 44 hours later.

Co-immunoprecipitation and immunoblotting. Co-immunoprecipitation was performed in COS-7 cells. Cells were grown in Dulbecco's modified Eagle's medium supplemented with 10% fetal bovine serum. At 90% confluency, 10-cm plates were

transfected with HA-Irx3, FLAG- Nkx2-5, HA-Tbx5, and HA-Su(fu) constructs and Lipofectamine 2000 (Invitrogen). After 32 days post transfection, cells were harvested with lysis buffer (150 mM NaCl, 1 mM EGTA and 1% Triton X-100). Cell lysates were incubated with the indicated antibodies overnight at 4°C; immunoprecipitates were pulled down with protein G–Sepharose beads and immunoblotted with the indicated antibodies for overnight at 4°C, following standard protocols.

Chromatin immunoprecipitation.

Chromatin was isolated from hearts expressing *Irx3*^{3myc6his}. The Imprint Chromatin Immunoprecipitation Kit (Sigma) was used according to manufacturer's instructions to capture Myc-tagged Irx3 protein. DNA fragments were analyzed by qPCR using custom Taqman assays specific to regions of interest. For the Nppa proximal promoter, the primers used are: 5'-GGGACCACCACATATTTCATGCT-3', and 5'-GTGTCCAAGGTGCCAACAG-3'. For intergenic *Gja1*: 5'-GGACAGACATCTGCCAAGGT-3', and 5'-ATGCCCCTCAGCTATCACAC-3'. For *Gja1* core promoter: 5'- GCCCCTCCTTCCAGTTGAG-3', and 5'-TTTTTAACTTGGAGCACAGAGCTTT-3'. For the conserved binding site: 5'-GGTCTGGTTGTGAAATGCCTTT-3', and R 5'-CTCTTCCTCTTAAACCCGGACAATT-3'.

Quantitative PCR.

Total RNA was isolated with TRIZOL reagent (Invitrogen), and cDNA was synthesized from 1.5 μg of RNA with Superscript II reverse transcriptase (Invitrogen). Taqman and

SYBR Green PCR methods were carried out using ABI 7900HT (Applied Biosystems). Primers and probes for mouse *Irx3*, *Gja5*, *Gja1*, and *GAPDH* are as follows:

Irx3 forward, 5'-GGCCGCCTCTGGGTCCCTAT-3'; reverse, 5'-GAGCGCCCAGCTGTGGGAAG-3';

Gja5 forward, 5'-AAGCAGAAGGCTCGGCCTC-3'; reverse, 5'-GGAAGCTCCAGTCACCCATCTT-3';

Gja1 forward, 5'-TCATTAAGTGAAAGAGAGGTGCCC-3'; reverse, 5'-TGGAGTAGGCTTGGACCTTGTC-3'; GAPDH, TaqMan Rodent GAPDH Control Reagents.

FACS.

FACS sorting of single cells isolated from *Irx3::EGFP*+ ventricles was carried out using FACSDiva and FlowJo. The Irx3::EGFP BAC line was obtained from the Gene Expression Nervous System Atlas (GENSAT) Project, NINDS Contracts N01NS02331 & HHSN271200723701C to The Rockefeller University (New York, NY).

Statistical analysis.

Differences between groups were examined for statistical significance by using the student's t-test. P values of <0.05 were regarded as significant.

BIBLIOGRAPHY

Aanhaanen WT, Mommersteeg MT, Norden J, Wakker V, de Gier-de Vries C, Anderson RH, Kispert A, Moorman AF, Christoffels VM. 2010. Developmental origin, growth, and three-dimensional architecture of the atrioventricular conduction axis of the mouse heart. *Circ Res* **107**: 728-736.

An RH, Wang XL, Kerem B, Benhorin J, Medina A, Goldmit M, Kass RS. 1998. Novel LQT-3 mutation affects Na+ channel activity through interactions between alpha- and beta1-subunits. *Circ Res* **83**: 141-146.

Bakker ML, Boukens BJ, Mommersteeg MT, Brons JF, Wakker V, Moorman AF, Christoffels VM. 2008. Transcription factor Tbx3 is required for the specification of the atrioventricular conduction system. *Circ Res* **102**: 1340-1349.

Bao ZZ, Bruneau BG, Seidman JG, Seidman CE, Cepko CL. 1999. Regulation of chamber-specific gene expression in the developing heart by Irx4. *Science (New York, NY* **283**: 1161-1164.

Berger MF, Badis G, Gehrke AR, Talukder S, Philippakis AA, Pena-Castillo L, Alleyne TM, Mnaimneh S, Botvinnik OB, Chan ET et al. 2008. Variation in homeodomain DNA binding revealed by high-resolution analysis of sequence preferences. *Cell* **133**: 1266-1276.

Bevilacqua LM, Simon AM, Maguire CT, Gehrmann J, Wakimoto H, Paul DL, Berul CI. 2000. A targeted disruption in connexin40 leads to distinct atrioventricular conduction defects. *J Interv Card Electrophysiol* **4**: 459-467.

Bilioni A, Craig G, Hill C, McNeill H. 2005. Iroquois transcription factors recognize a unique motif to mediate transcriptional repression in vivo. *Proc Natl Acad Sci U S A* **102**: 14671-14676.

Boukens BJ, Christoffels VM, Coronel R, Moorman AF. 2009. Developmental basis for electrophysiological heterogeneity in the ventricular and outflow tract myocardium as a substrate for life-threatening ventricular arrhythmias. *Circ Res* **104**: 19-31.

Bruneau BG, Bao ZZ, Fatkin D, Xavier-Neto J, Georgakopoulos D, Maguire CT, Berul CI, Kass DA, Kuroski-de Bold ML, de Bold AJ et al. 2001. Cardiomyopathy in Irx4-deficient mice is preceded by abnormal ventricular gene expression. *Mol Cell Biol* **21**: 1730-1736.

Callahan CA, Thomas JB. 1994. Tau-beta-galactosidase, an axon-targeted fusion protein. *Proc Natl Acad Sci U S A* **91**: 5972-5976.

Castellanos A, Jr., Maytin O, Arcebal AG, Lemberg L. 1970. Significance of complete right bundle-branch block with right axis deviation in absence of right ventricular hypertrophy. *Br Heart J* **32**: 85-92.

Cavodeassi F, Modolell J, Gomez-Skarmeta JL. 2001. The Iroquois family of genes: from body building to neural patterning. *Development (Cambridge, England)* **128**: 2847-2855.

Cheng G, Litchenberg WH, Cole GJ, Mikawa T, Thompson RP, Gourdie RG. 1999. Development of the cardiac conduction system involves recruitment within a multipotent cardiomyogenic lineage. *Development* **126**: 5041-5049.

Chi NC, Shaw RM, Jungblut B, Huisken J, Ferrer T, Arnaout R, Scott I, Beis D, Xiao T, Baier H et al. 2008. Genetic and physiologic dissection of the vertebrate cardiac conduction system. *PLoS Biol* **6**: e109.

Christoffels VM, Keijser AG, Houweling AC, Clout DE, Moorman AF. 2000. Patterning the embryonic heart: identification of five mouse Iroquois homeobox genes in the developing heart. *Dev Biol* **224**: 263-274.

Cohen DR, Cheng CW, Cheng SH, Hui CC. 2000. Expression of two novel mouse Iroquois homeobox genes during neurogenesis. *Mech Dev* **91**: 317-321.

Cohen SI, Lau SH, Stein E, Young MW, Damato AN. 1968. Variations of aberrant ventricular conduction in man: evidence of isolated and combined block within the specialized conduction system. An electrocardiographic and vectorcardiographic study. *Circulation* **38**: 899-916.

Cole WC, Picone JB, Sperelakis N. 1988. Gap junction uncoupling and discontinuous propagation in the heart. A comparison of experimental data with computer simulations. *Biophysical journal* **53**: 809-818.

Costantini DL, Arruda EP, Agarwal P, Kim KH, Zhu Y, Zhu W, Lebel M, Cheng CW, Park CY, Pierce SA et al. 2005. The homeodomain transcription factor Irx5 establishes the mouse cardiac ventricular repolarization gradient. *Cell* **123**: 347-358.

Cottrell GT, Burt JM. 2001. Heterotypic gap junction channel formation between heteromeric and homomeric Cx40 and Cx43 connexons. *Am J Physiol Cell Physiol* **281**: C1559-1567.

-. 2005. Functional consequences of heterogeneous gap junction channel formation and its influence in health and disease. *Biochim Biophys Acta* **1711**: 126-141.

Danielian PS, Muccino D, Rowitch DH, Michael SK, McMahon AP. 1998. Modification of gene activity in mouse embryos in utero by a tamoxifen-inducible form of Cre recombinase. *Curr Biol* **8**: 1323-1326.

Delorme B, Dahl E, Jarry-Guichard T, Briand JP, Willecke K, Gros D, Theveniau-Ruissy M. 1997. Expression pattern of connexin gene products at the early developmental stages of the mouse cardiovascular system. *Circ Res* **81**: 423-437.

Dhar Malhotra J, Chen C, Rivolta I, Abriel H, Malhotra R, Mattei LN, Brosius FC, Kass RS, Isom LL. 2001. Characterization of sodium channel alpha- and beta-subunits in rat and mouse cardiac myocytes. *Circulation* **103**: 1303-1310.

Dhingra R, Pencina MJ, Wang TJ, Nam BH, Benjamin EJ, Levy D, Larson MG, Kannel WB, D'Agostino RB, Sr., Vasan RS. 2006. Electrocardiographic QRS duration and the risk of congestive heart failure: the Framingham Heart Study. *Hypertension* **47**: 861-867.

Dominguez JN, Navarro F, Franco D, Thompson RP, Aranega AE. 2005. Temporal and spatial expression pattern of beta1 sodium channel subunit during heart development. *Cardiovasc Res* **65**: 842-850.

Fast VG, Kleber AG. 1995a. Block of impulse propagation at an abrupt tissue expansion: evaluation of the critical strand diameter in 2- and 3-dimensional computer models. *Cardiovasc Res* **30**: 449-459.

-. 1995b. Cardiac tissue geometry as a determinant of unidirectional conduction block: assessment of microscopic excitation spread by optical mapping in patterned cell cultures and in a computer model. *Cardiovasc Res* **29**: 697-707.

Gaborit N, Le Bouter S, Szuts V, Varro A, Escande D, Nattel S, Demolombe S. 2007. Regional and tissue specific transcript signatures of ion channel genes in the non-diseased human heart. *J Physiol* **582**: 675-693.

Gehrmann J, Berul CI. 2000. Cardiac electrophysiology in genetically engineered mice. *J Cardiovasc Electrophysiol* **11**: 354-368.

Gittenberger-de Groot AC, Blom NM, Aoyama N, Sucov H, Wenink AC, Poelmann RE. 2003. The role of neural crest and epicardium-derived cells in conduction system formation. *Novartis Found Symp* **250**: 125-134; discussion 134-141, 276-129.

Gomez-Skarmeta JL, Diez del Corral R, de la Calle-Mustienes E, Ferre-Marco D, Modolell J. 1996. Araucan and caupolican, two members of the novel iroquois complex, encode homeoproteins that control proneural and vein-forming genes. *Cell* **85**: 95-105.

Gomez-Skarmeta JL, Modolell J. 1996. araucan and caupolican provide a link between compartment subdivisions and patterning of sensory organs and veins in the Drosophila wing. *Genes & development* **10**: 2935-2945.

-. 2002. Iroquois genes: genomic organization and function in vertebrate neural development. *Curr Opin Genet Dev* **12**: 403-408.

Gourdie RG, Severs NJ, Green CR, Rothery S, Germroth P, Thompson RP. 1993. The spatial distribution and relative abundance of gap-junctional connexin40 and

connexin43 correlate to functional properties of components of the cardiac atrioventricular conduction system. *J Cell Sci* **105 (Pt 4)**: 985-991.

Gutyon, Arthur C, and Hall, John E. (2005). Unit II: Membrane physiology, nerve and muscle. Textbook of medical physiology. (pp. 43-100). Philidelphia, PA: Saunders Book Company.

Gutyon, Arthur C, and Hall, John E. (2005). Unit II: Membrane physiology, nerve and muscle. Textbook of medical physiology. (pp. 101-158). Philidelphia, PA: Saunders Book Company.

Hoffman JI, Kaplan S. 2002. The incidence of congenital heart disease. *Journal of the American College of Cardiology* **39**: 1890-1900.

Hoogaars WM, Tessari A, Moorman AF, de Boer PA, Hagoort J, Soufan AT, Campione M, Christoffels VM. 2004. The transcriptional repressor Tbx3 delineates the developing central conduction system of the heart. *Cardiovasc Res* **62**: 489-499.

Isom LL. 2001. Sodium channel beta subunits: anything but auxiliary. *Neuroscientist* **7**: 42-54.

Iuliano S, Fisher SG, Karasik PE, Fletcher RD, Singh SN. 2002. QRS duration and mortality in patients with congestive heart failure. *Am Heart J* **143**: 1085-1091.

Jongsma HJ, Wilders R. 2000. Gap junctions in cardiovascular disease. *Circ Res* **86**: 1193-1197.

Jordan KC, Clegg NJ, Blasi JA, Morimoto AM, Sen J, Stein D, McNeill H, Deng WM, Tworoger M, Ruohola-Baker H. 2000. The homeobox gene mirror links EGF signalling to embryonic dorso-ventral axis formation through notch activation. *Nature genetics* **24**: 429-433.

Kehl BT, Cho KO, Choi KW. 1998. mirror, a Drosophila homeobox gene in the Iroquois complex, is required for sensory organ and alula formation. *Development (Cambridge, England)* **125**: 1217-1227.

Kirchhoff S, Nelles E, Hagendorff A, Kruger O, Traub O, Willecke K. 1998. Reduced cardiac conduction velocity and predisposition to arrhythmias in connexin40-deficient mice. *Curr Biol* **8**: 299-302.

Kleber AG, Rudy Y. 2004. Basic mechanisms of cardiac impulse propagation and associated arrhythmias. *Physiol Rev* **84**: 431-488.

Kreuzberg MM, Schrickel JW, Ghanem A, Kim JS, Degen J, Janssen-Bienhold U, Lewalter T, Tiemann K, Willecke K. 2006. Connexin30.2 containing gap junction channels decelerate impulse propagation through the atrioventricular node. *Proc Natl Acad Sci U S A* **103**: 5959-5964.

Lisewski U, Shi Y, Wrackmeyer U, Fischer R, Chen C, Schirdewan A, Juttner R, Rathjen F, Poller W, Radke MH et al. 2008. The tight junction protein CAR regulates cardiac conduction and cell-cell communication. *J Exp Med* **205**: 2369-2379.

Maguire CT, Bevilacqua LM, Wakimoto H, Gehrmann J, Berul CI. 2000. Maturational atrioventricular nodal physiology in the mouse. *Journal of cardiovascular electrophysiology* **11**: 557-564.

Mangoni ME, Nargeot J. 2008. Genesis and regulation of the heart automaticity. *Physiol Rev* **88**: 919-982.

Matsumoto K, Nishihara S, Kamimura M, Shiraishi T, Otoguro T, Uehara M, Maeda Y, Ogura K, Lumsden A, Ogura T. 2004. The prepattern transcription factor Irx2, a

target of the FGF8/MAP kinase cascade, is involved in cerebellum formation. *Nat Neurosci* **7**: 605-612.

McNeill H, Yang CH, Brodsky M, Ungos J, Simon MA. 1997. mirror encodes a novel PBX-class homeoprotein that functions in the definition of the dorsal-ventral border in the Drosophila eye. *Genes & development* **11**: 1073-1082.

Meysen S, Marger L, Hewett KW, Jarry-Guichard T, Agarkova I, Chauvin JP, Perriard JC, Izumo S, Gourdie RG, Mangoni ME et al. 2007. Nkx2.5 cell-autonomous gene function is required for the postnatal formation of the peripheral ventricular conduction system. *Dev Biol* **303**: 740-753.

Mikawa T, Hurtado R. 2007. Development of the cardiac conduction system. *Semin Cell Dev Biol* **18**: 90-100.

Miquerol L, Dupays L, Theveniau-Ruissy M, Alcolea S, Jarry-Guichard T, Abran P, Gros D. 2003. Gap junctional connexins in the developing mouse cardiac conduction system. *Novartis Found Symp* **250**: 80-98; discussion 98-109, 276-109.

Miquerol L, Meysen S, Mangoni M, Bois P, van Rijen HV, Abran P, Jongsma H, Nargeot J, Gros D. 2004. Architectural and functional asymmetry of the His-Purkinje system of the murine heart. *Cardiovasc Res* **63**: 77-86.

Mond HG. 2006. The world survey of cardiac pacing and cardioverter-defibrillators: lessons learnt. *J Interv Card Electrophysiol* **17**: 211-214.

Morley GE, Vaidya D. 2001. Understanding conduction of electrical impulses in the mouse heart using high-resolution video imaging technology. *Microsc Res Tech* **52**: 241-250.

Morley GE, Vaidya D, Jalife J. 2000. Characterization of conduction in the ventricles of normal and heterozygous Cx43 knockout mice using optical mapping. *Journal of cardiovascular electrophysiology* **11**: 375-377.

Moskowitz IP, Kim JB, Moore ML, Wolf CM, Peterson MA, Shendure J, Nobrega MA, Yokota Y, Berul C, Izumo S et al. 2007. A molecular pathway including Id2, Tbx5, and Nkx2-5 required for cardiac conduction system development. *Cell* **129**: 1365-1376.

Mummenhoff J, Houweling AC, Peters T, Christoffels VM, Ruther U. 2001. Expression of Irx6 during mouse morphogenesis. *Mech Dev* **103**: 193-195.

Myerburg RJ. 1971. The gating mechanism in the distal atrioventricular conducting system. *Circulation* **43**: 955-960.

Nakamura T, Colbert MC, Robbins J. 2006. Neural crest cells retain multipotential characteristics in the developing valves and label the cardiac conduction system. *Circ Res* **98**: 1547-1554.

Noyes MB, Christensen RG, Wakabayashi A, Stormo GD, Brodsky MH, Wolfe SA. 2008. Analysis of homeodomain specificities allows the family-wide prediction of preferred recognition sites. *Cell* **133**: 1277-1289.

Nygren A, Clark RB, Belke DD, Kondo C, Giles WR, Witkowski FX. 2000. Voltage-sensitive dye mapping of activation and conduction in adult mouse hearts. *Ann Biomed Eng* **28**: 958-967.

Reggiani L, Raciti D, Airik R, Kispert A, Brandli AW. 2007. The prepattern transcription factor Irx3 directs nephron segment identity. *Genes & development* **21**: 2358-2370.

Remme CA, Verkerk AO, Hoogaars WM, Aanhaanen WT, Scicluna BP, Annink C, van den Hoff MJ, Wilde AA, van Veen TA, Veldkamp MW et al. 2009. The cardiac sodium channel displays differential distribution in the conduction system and transmural heterogeneity in the murine ventricular myocardium. *Basic Res Cardiol* **104**: 511-522.

Rudy Y. 1998. Cardiac conduction: an interplay between membrane and gap junction. *J Electrocardiol* **31 Suppl**: 1-5.

-. 2005. Lessons learned about slow discontinuous conduction from models of impulse propagation. *J Electrocardiol* **38**: 52-54.

Rudy Y, Shaw RM. 1997. Cardiac excitation: an interactive process of ion channels and gap junctions. *Adv Exp Med Biol* **430**: 269-279.

Saez JC, Berthoud VM, Branes MC, Martinez AD, Beyer EC. 2003. Plasma membrane channels formed by connexins: their regulation and functions. *Physiol Rev* **83**: 1359-1400.

Schram G, Pourrier M, Melnyk P, Nattel S. 2002. Differential distribution of cardiac ion channel expression as a basis for regional specialization in electrical function. *Circ Res* **90**: 939-950.

Sedmera D, Reckova M, DeAlmeida A, Coppen SR, Kubalak SW, Gourdie RG, Thompson RP. 2003a. Spatiotemporal pattern of commitment to slowed proliferation in the embryonic mouse heart indicates progressive differentiation of the cardiac conduction system. *The anatomical record* **274**: 773-777.

Sedmera D, Reckova M, deAlmeida A, Sedmerova M, Biermann M, Volejnik J, Sarre A, Raddatz E, McCarthy RA, Gourdie RG et al. 2003b. Functional and

morphological evidence for a ventricular conduction system in zebrafish and Xenopus hearts. *Am J Physiol Heart Circ Physiol* **284**: H1152-1160.

Sharpe J, Ahlgren U, Perry P, Hill B, Ross A, Hecksher-Sorensen J, Baldock R, Davidson D. 2002. Optical projection tomography as a tool for 3D microscopy and gene expression studies. *Science* **296**: 541-545.

Shaw RM, Rudy Y. 1997. Ionic mechanisms of propagation in cardiac tissue. Roles of the sodium and L-type calcium currents during reduced excitability and decreased gap junction coupling. *Circ Res* **81**: 727-741.

Silverman ME, Grove D, Upshaw CB, Jr. 2006. Why does the heart beat? The discovery of the electrical system of the heart. *Circulation* **113**: 2775-2781.

Simon AM, Goodenough DA, Paul DL. 1998. Mice lacking connexin40 have cardiac conduction abnormalities characteristic of atrioventricular block and bundle branch block. *Curr Biol* **8**: 295-298.

Srivastava D. 2006. Making or breaking the heart: from lineage determination to morphogenesis. *Cell* **126**: 1037-1048.

St Amand TR, Lu JT, Zamora M, Gu Y, Stricker J, Hoshijima M, Epstein JA, Ross JJ, Jr., Ruiz-Lozano P, Chien KR. 2006. Distinct roles of HF-1b/Sp4 in ventricular and neural crest cells lineages affect cardiac conduction system development. *Dev Biol* **291**: 208-217.

Tamaddon HS, Vaidya D, Simon AM, Paul DL, Jalife J, Morley GE. 2000. High-resolution optical mapping of the right bundle branch in connexin40 knockout mice reveals slow conduction in the specialized conduction system. *Circ Res* **87**: 929-936.

Thomas PS, Kasahara H, Edmonson AM, Izumo S, Yacoub MH, Barton PJ, Gourdie RG. 2001. Elevated expression of Nkx-2.5 in developing myocardial conduction cells. *Anat Rec* **263**: 307-313.

Valiunas V, Gemel J, Brink PR, Beyer EC. 2001. Gap junction channels formed by coexpressed connexin40 and connexin43. *Am J Physiol Heart Circ Physiol* **281**: H1675-1689.

van Tuyl M, Liu J, Groenman F, Ridsdale R, Han RN, Venkatesh V, Tibboel D, Post M. 2006. Iroquois genes influence proximo-distal morphogenesis during rat lung development. *American journal of physiology* **290**: L777-L789.

van Veen AA, van Rijen HV, Opthof T. 2001. Cardiac gap junction channels: modulation of expression and channel properties. *Cardiovasc Res* **51**: 217-229.

van Veen TA, van Rijen HV, van Kempen MJ, Miquerol L, Opthof T, Gros D, Vos MA, Jongsma HJ, de Bakker JM. 2005. Discontinuous conduction in mouse bundle branches is caused by bundle-branch architecture. *Circulation* **112**: 2235-2244.

Verzi MP, McCulley DJ, De Val S, Dodou E, Black BL. 2005. The right ventricle, outflow tract, and ventricular septum comprise a restricted expression domain within the secondary/anterior heart field. *Dev Biol* **287**: 134-145.

Viragh S, Challice CE. 1982. The development of the conduction system in the mouse embryo heart. *Dev Biol* **89**: 25-40.

Zhang SS and Bruneau BG. (2007). Transcriptional control of the cardiac conduction system. *Advances in Developmental Biology, Cardiovascular Development, 18*. Chapter 10, Amsterdam: Elsevier Science.

Zhou YQ, Foster FS, Nieman BJ, Davidson L, Chen XJ, Henkelman RM. 2004. Comprehensive transthoracic cardiac imaging in mice using ultrasound biomicroscopy with anatomical confirmation by magnetic resonance imaging. *Physiol Genomics* **18**: 232-244.

PUBLISHING AGREEMENT

It is the policy of the University to encourage the distribution of all theses, dissertations, and manuscripts. Copies of all UCSF theses, dissertations, and manuscripts will be routed to the library via the Graduate Division. The library will make all theses, dissertations, and manuscripts accessible to the public and will preserve these to the best of their abilities, in perpetuity.

Please sign the following statement:

I hereby grant permission to the Graduate Division of the University of California, San Francisco to release copies of my thesis, dissertation, or manuscript to the Campus Library to provide access and preservation, in whole or in part, in perpetuity.

12. 15. 2010

Author Signature

Date